ABSTRACT

Title of thesis: DYNAMIC FORCE MEASUREMENT CAPABILITIES FOR HYPERSONIC WIND TUNNEL TESTING

Arianne Xaviera Collopy, Master of Science, 2015

Thesis directed by: Professor Sung W. Lee
Department of Aerospace Engineering

The object of this research is to characterize a new hybrid force measurement methodology using a piezoelectric balance in parallel with a conventional strain gauge balance, with the goal of enabling wide frequency range measurements for use in hypersonic ground test facilities. This technology, developed in collaboration with the Hypervelocity Wind Tunnel 9 at AEDC in White Oak, Maryland, is expected to provide accurate static and dynamic force and moment measurements on conventional test articles, providing simultaneous force, moment, heat transfer, and pressure measurements for maximal test productivity.

A finite element model of the model-balance-sting assembly was developed to perform static and transient simulations and thereby characterize the influence of design parameters such as model weight, stiffness, and placement of load cells. This thesis describes the work done with the computational model, paralleling ongoing laboratory work, which includes development of methodologies for static calibration and dynamic calibration using acceleration compensation.

DYNAMIC FORCE MEASUREMENT CAPABILITIES FOR HYPERSONIC WIND TUNNEL TESTING

by

Arianne Xaviera Collopy

Thesis submitted to the Faculty of the Graduate School of the
University of Maryland, College Park in partial fulfillment
of the requirements for the degree of
Master of Science
2015

Advisory Committee:
Professor Sung W. Lee, Chair
Professor Norman M. Wereley
Professor Inderjit Chopra
Dr. Eric C. Marineau

Acknowledgments

I would like to thank my adviser Sung Lee for continued insightful discussions and guidance in my research. My officemates at Maryland, Erick Butzlaff, Ananth Virakthi, and James Briscoe, have proven incredibly valuable resources, particularly regarding discussions of theory and Abaqus modeling. I would also like to acknowledge the time that Mary Bowden and Alison Flatau have taken to mentor me as a teaching assistant and a graduate student.

I would like to extend thanks to the employees at Tunnel 9, especially Eric Marineau, John Lafferty, and Dan Marren, for providing laboratory space, resources, and tremendously helpful knowledge. The Hypersonic Center of Testing Excellence led by Ken Yu and Mark Lewis at Maryland was incredibly instrumental to see the broader scope of my research and as a platform to learn from my colleagues.

My inspiration to do quality work and writing comes from Deirdre O'Carroll, and I cannot thank her enough for her mentorship. George Hazelrigg deserves sincere thanks for a thoughtful discussion over doughnuts on what it means to validate a model – I recall it often. Finally, I would like to thank my family and friends who have always lent an ear to bounce ideas off of; I would not be where I am without you.

This work is funded through grant FA9101-10-D-0001 at Arnold Engineering Development Center Hypervelocity Tunnel 9 in White Oak, Maryland.

Table of Contents

List of Tables

List of Figures

Chapter 1: Introduction

One of the major challenges in developing dynamic force measurement tools for use in a hypervelocity blowdown wind tunnel is the reduced test time as compared to low-speed wind tunnels which may be operated continuously. In low-speed tunnels, the test article has time to come to equilibrium during the duration of the test and therefore pressure and drag loads on the article can be straightforwardly measured. For high speed wind tunnels, pressure and drag loads are much more difficult to separate from vibration of the test article or model support structure. Therefore, an important research goal is whether high frequency force measurement can contribute to the accurate measurement of impulsive loads for models in a hypervelocity wind tunnel.

In many cases, the load measurement tool employed in wind tunnel testing is a strain gauge force balance, as this technology is proven to give accurate measurements at low frequency. The frequency response of conventional strain gauge balances is typically below 30 Hz so that the high sensitivity and low crosstalk requirements for this measurement system are met, however this range is insufficient for accurate measurement of transient loads incurred during impulsive events. A high frequency measurement tool is needed to characterize loads on test articles

associated with events such as the unstart of scramjet inlets [1, 2], mode switching [3], shroud separation [1,4,5], stage separation [6], and divert thrusters firing [7]. These dynamic events involve large unsteady forces on millisecond time scales and are generated by complex flow physics such as shock interaction and boundary layer separation, both of which pose considerable modeling challenges and are active areas of research [12]. Because large uncertainties exist when computing these complex flows, accurate measurement of unsteady forces and moments in ground test facilities is essential to reduce the risks during development of hypersonic systems.

1.1 Research Question

This thesis presents work towards the research goal stated above by investigating two specific questions:

1. How can a static calibration methodology be developed using high frequency force measurements to recover static loads in an abstract case as well as the case of a generic test article?

2. How should the development of a similar methodology for recovery of transient forces and moments be approached?

This work therefore consists of studies to look at the effects of test article design parameters as well as sensor placement on the ability to recover static and dynamic forces and moments. The majority of the work presented herein is computational, aided by commercial finite element tools, and presents a testbed for sensitivity analyses to assess various design parameters. For this work, experimental facilities

are provided by Arnold Engineering Development Center (AEDC) in White Oak, Maryland, home of AEDC's Hypervelocity Tunnel 9, which is capable of Mach 14 air flow and continuous pitch sweep [13]. Further laboratory work to corroborate the computational model is an ongoing effort between the University of Maryland and Tunnel 9.

1.2 Outline

In Chapter 2, a novel high frequency force balance system is presented along with a review of past research that provides a foundation for this work. In Chapter 3, the first research question is partially answered with a discussion of the development of a static calibration methodology as applied to an abstract case. Section 3.7 extends this methodology to a generic test article, thus concluding the first research question. The answer to the second research question is found in Chapter 4, where an approach is considered for the extension of the calibration methodology described herein to the case of transient load recovery. Recommendations for future work are included in Chapter 5.

Chapter 2: Literature Review

This literature review covers current force measurement technology, both for high frequency and low frequency applications. Following this introduction, previous use of these measurement technologies for high-speed wind tunnel testing is described. Next, this thesis is placed in context relative to the previous work and the specific test article used in the thesis is described.

2.1 Force Balances

The most common measurement tool for recording forces on test articles in ground test facilities is a strain gauge balance, accurate and extremely reliable for quasi-static loads. The restriction to the quasi-static regime is due to the frequency limitation of the measurement system based on the stiffness requirements of the balance itself to minimize crosstalk between orthogonal sensor components. This means that typical strain gauge balances are not suitable for measurement of high frequency inertial loads, however we continue to use a strain gauge balance in our proposed force balance hardware because it is well-suited to low frequency measurement, thus allowing broadband measurement.

2.2 Piezoelectrics

Piezoelectricity is an intrinsic and reversible mechanical property of a few types of crystals where electric charges accumulate in a crystal due to applied strain. This accumulation of charge upon force application can be measured as voltage. This effect typically occurs along material axes, defined by the crystallographic planes of the material, which allows for selective measurement of loads along these axes. In contrast to many common force sensors, including strain gauge force sensors, this property allows for a simpler sensor design: these materials can directly measure force and do not require separate sensing and transduction elements [14]. This combination of simplicity, stiffness, and high sensitivity makes piezoelectric sensors ideal for our application.

2.3 Past Work

A prototype force balance utilizing piezoelectric force sensors was designed for the high-enthalpy and extremely short test times in the LENS-XX reflected shock tunnel, and further implemented successfully on a reentry capsule tested in the Mach 9 expansion tunnel at CUBRC [9]. To complement the high frequency force measurements, high-frequency acceleration measurements can be made, which allows for calculation of inertial loads due to vibrations of the test article. This technique, denoted acceleration compensation, was introduced with the piezoelectric force measurement system and excellent agreement was found between simulations and acceleration compensated strain gauge results presented by Marineau *et al* in

2012 [10], as well as increased accuracy over previous capsule measurements from Störkmann *et al* [11].

Drawing on these successes, a new hybrid force balance system is presented in this thesis. The hybrid system consists of high frequency piezoelectric force sensors in parallel with conventional low frequency strain gauge measurements. The goal of this system is to enable accurate determination of both dynamic loading as well as quasi-static forces and moments for a full frequency characterization. A step towards this goal is the subject of this thesis, which covers static calibration methodology and a plan for dynamic calibration methodology using this hybrid force balance.

2.4 Test Article and Rationale

The generic test article designed for this work, shown in Figure 2.1, was designed to facilitate development of the hybrid force balance technology and has dimensions, weight, inertia, and natural frequencies similar to typical Tunnel 9 test articles. The orthogonal surfaces will facilitate the attachment of single-component calibration weights and accelerometers at known positions and orientations. The number and location of points where calibration loads are applied and accelerometers are located can be determined from computational sensitivity analyses.

For these analyses, the strain gauge will be replaced with a rigid steel bar as a dummy balance, machined to match the dimensions of the true balance. This is done to evaluate the piezoelectric balance alone in preliminary studies, and the true strain gauge balance may be incorporated in later studies. The devised balance assembly architecture is shown in Figure 2.2.

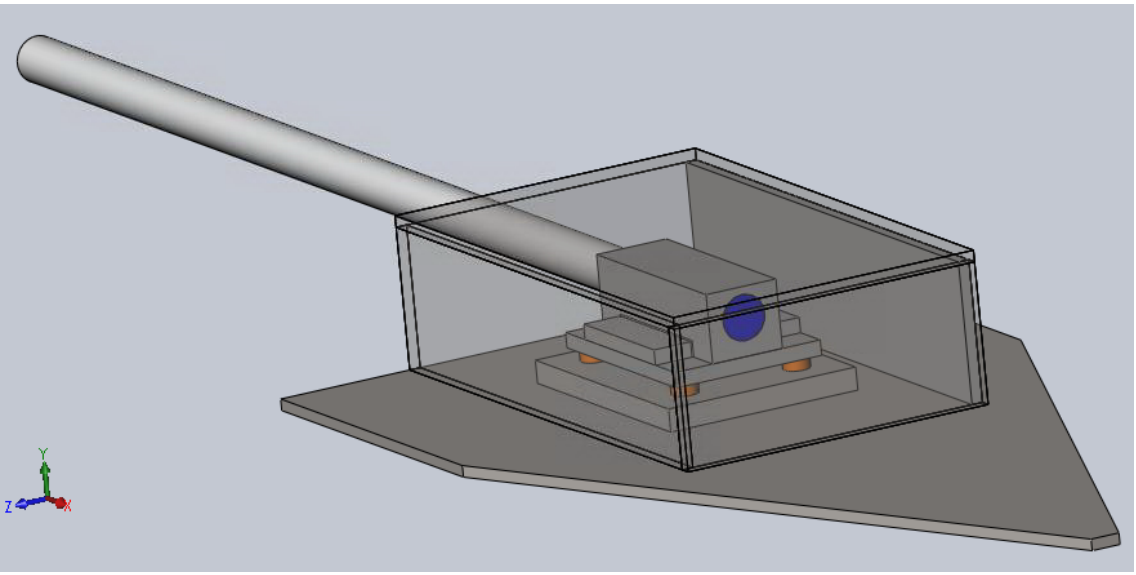

Figure 2.1. SolidWorks model of custom test article

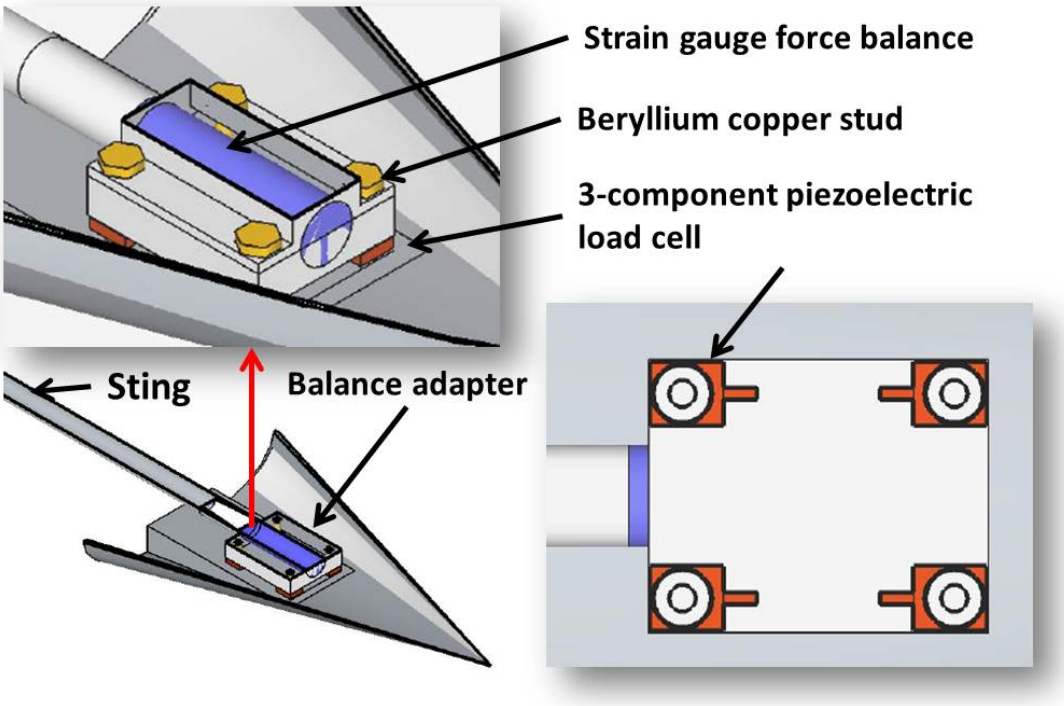

Figure 2.2. New hybrid force balance concept

Chapter 3: Static Calibration

The calibration procedures for a force balance result in a calibration matrix that ideally can be used to recover any unknown loading on a test article during a test by relating sensor measurements to applied forces and moments. For use in dynamic force measurements, both static and dynamic calibration matrices are required - the former for recovery of instantaneous loading and the latter providing a correlation between acceleration measurements and dynamic force profiles. There are several challenges of determining an accurate calibration methodology, perhaps the most important of which is the simple fact that the calibration load schedules are individual point loads, whereas the expected loads during a wind tunnel test are generally shear or pressure distributions. Since calibrating loads at every point on a model is unreasonable, it is a worthwhile exercise to determine whether certain points on the model or a specific arrangement of load locations add to the ability of the calibration matrix to recover unknown loads. Here, we examine the effects of load schedule and test article design on errors in force and moment recovery.

3.1 Computational Analysis

The simplified model used for static calibration tests, shown in Figure 3.1, is comprised of two steel plates of thickness 25.4 mm and 100 mm on each side, with all translational degrees of freedom fully constrained on the bottom surface. Four toroidal quartz sensors are sandwiched between the two plates at a center-to-center spacing of 0.065 mm, approximately the maximum spacing that is allowed by the force sensor hardware enclosure. For the case of the computational model, this enclosure is omitted as the contact surfaces are designed to be only those areas directly above and below the cylindrical force sensors themselves, so this omission is consistent with the hardware operation. Note that for all of these analyses, the shear force components are F_x and F_z, and the normal force component is F_y, as indicated by the coordinate system drawn in Figure 3.1.

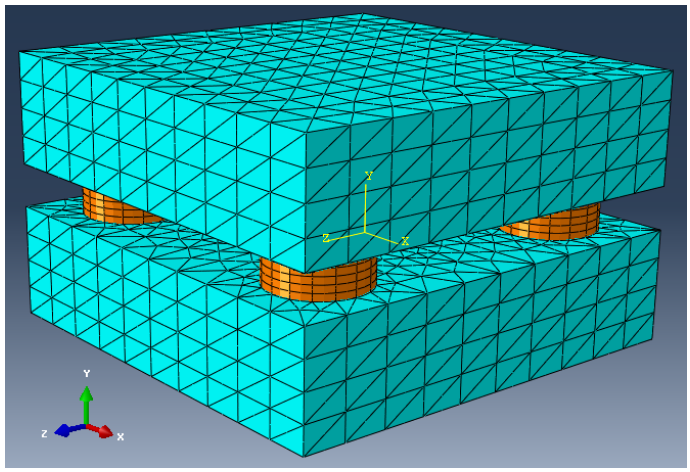

Figure 3.1. Mesh of simplied 2-plate geometry; sensor elements highlighted in orange

The numerical analysis was performed using Abaqus commercial finite element software in conjunction with MATLAB for processing of output data. The finite

element model is mostly formed of quadratic tetrahedral (C3D10) elements, with the piezo sensor modeled by quadratic prism (C3D15) elements. For this model and all subsequent models presented herein, part interactions are fully tied, equating displacements at matching nodes across part boundaries. This use of a surface constraint rather than modeling connections between parts allows for a simple characterization of part interactions. Three-component nodal force data is extracted from each surface of the toroidal sensor elements. For the case of ideal sensors, this force output is directly proportional to the device's measured voltage output.

This simplified model was chosen for its ease of modeling as well as its simplicity; the high symmetry allows for validation of computational results against expected behaviors. In addition, this model provides a way to isolate specific design properties such as plate thickness, sensor spacing, and material usage. The simplified model may also be easily updated in the future to investigate further design properties, such as a reduced number of sensors or asymmetry in the design.

Data was extracted from this model via nodal force measurement reports from the surface of each sensor. Checks were done internally throughout the analysis to ensure that all applied forces can be recovered and are consistent with free-body diagrams. The moment center is calculated as the midpoint between the four sensors, in the plane of the contacting upper surface of these sensor elements. Using this definition, the measured sensor data can be used to calculate resultant moment data by approximating the total force measured by each sensor as a single concentrated force at the center of each toroidal sensor element.

3.2 Calibration Methodology

Using a linear interaction model, N_C components of applied forces and moments can be related to each of N_S components of the measured force transducer outputs as in Equation 3.1. This is done for N distinct load cases, to give a $N \times N_C$ matrix of force components F and a $N \times N_S$ matrix of force sensor outputs S_F. An expression for the static calibration coefficient matrix C that relates the measured sensor data to known applied loads, therefore of size $N_S \times N_C$, directly follows and is shown in Equation 3.2.

$$F = S_F C \tag{3.1}$$

$$C = \left(S_F^T S_F\right)^{-1} S_F^T F \tag{3.2}$$

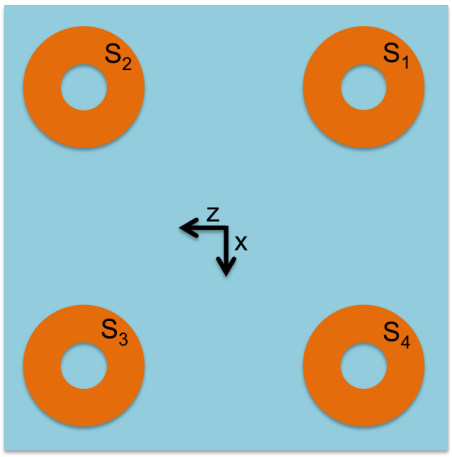

Figure 3.2. Cutaway schematic of sensor array for two-plate model

As an example, for a set of N three-component forces F applied at various calibration points to our sandwiched sensor array, we can first label the sensors as shown in Figure 3.2. Using this notation, Equation 3.1 expands to that described

in Equation 3.3, where both F and S_F are known, allowing for calculation of the unknown calibration matrix C. Note that for the case of three-component forces, the force-and-moment vector has $N_C = 6$ components, and for a system of four triaxial force sensors, there are $N_S = 12$ measured sensor outputs. Therefore our calibration matrix C has dimensions 12×6.

$$\begin{bmatrix} F_{x_1} & F_{y_1} & F_{z_1} & M_{x_1} & M_{y_1} & M_{z_1} \\ F_{x_2} & F_{y_2} & F_{z_2} & M_{x_2} & M_{y_2} & M_{z_2} \\ \vdots & & & & & \vdots \\ F_{x_N} & F_{y_N} & F_{z_N} & M_{x_N} & M_{y_N} & M_{z_N} \end{bmatrix}$$
$$= \begin{bmatrix} S_{1x_1} & S_{1y_1} & S_{1z_1} & S_{2x_1} & \dots & S_{4z_1} \\ S_{1x_2} & S_{1y_2} & S_{1z_2} & S_{2x_2} & \dots & S_{4z_2} \\ \vdots & & & & & \vdots \\ S_{1x_N} & S_{1y_N} & S_{1z_N} & S_{2x_N} & \dots & S_{4z_N} \end{bmatrix} \cdot \begin{bmatrix} C_{1,1} & C_{1,2} & \dots & C_{1,5} & C_{1,6} \\ \vdots & & & & \vdots \\ C_{12,1} & C_{12,2} & \dots & C_{12,5} & C_{12,6} \end{bmatrix} \tag{3.3}$$

The goal of this calibration process is therefore to have a robust calibration matrix such that any unknown forces can then be recovered from the force transducer measurements. Errors for all loads are calculated as $\epsilon = F - S_F C$, between the applied load F_j and those loads calculated from sensor data.

3.3 Sensitivity Analyses

This simplified model presented serves two main goals, the first of which is to serve as a preliminary testbed for development of the static calibration methodology, and the second is to run sensitivity analyses to determine the effects of design parameters on the accuracy of the resulting static calibration matrix. The parameters considered for these sensitivity analyses include load location arrangement, plate thickness, plate modulus, and sensor position with the goal of determining the effect these properties have on the accuracy of the static calibration matrix.

3.3.1 Load Locations

While it is important that the static calibration process accurately recovers those loads that go into the calibration procedure, as this indicates a well-fitted calibration curve, the resultant calibration matrix should also be universal such that any applied point load or distributed load may be recovered with good accuracy. Therefore several different load locations to define the input of the calibration matrix were examined, and the errors calculated for the recovery of both the input loads as well as varied pressure distributions.

Initially, three arrangements of potential load locations were considered, as shown in Figure 3.3, each including nine distinct points on the top surface of the upper plate. For each case, a series of 81 point loads were generated by using single-component loads in each of three coordinate directions at each of three magnitudes: 10N, 20N, and 40N, chosen to approximately span the range of typical loads used

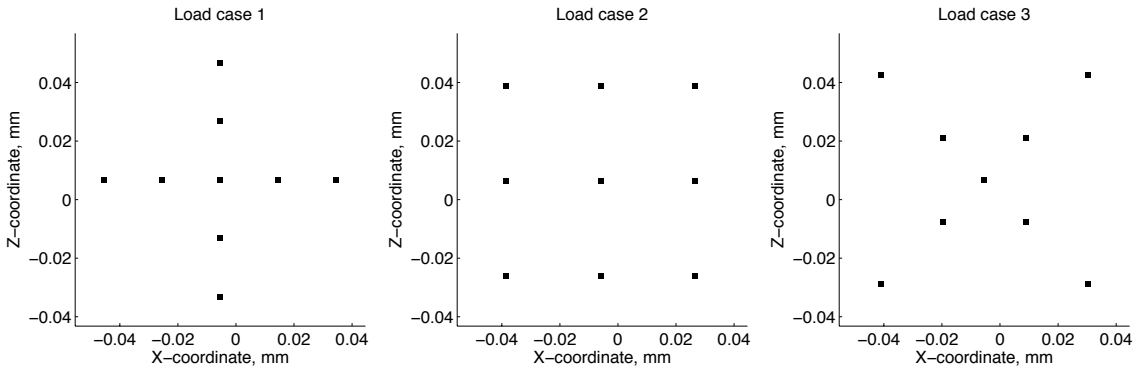

Figure 3.3. Load cases for static calibration tests on simplified plate model

for calibration. From these input loads, a calibration matrix was determined as in Equation 3.2. The errors between the actual applied load and the calculated load via the calibration matrix and force output for all six components of forces and moments are calculated and subsequently normalized by the euclidean norm of the applied force or moment vector, respectively. This normalization allows for verification of the linear nature of this system, as the normalized errors should (and do) agree for loads of varying magnitude, as seen in Figure 3.4. Plotted against the magnitude of applied loads, for the 81 loads used to generate the calibration matrix the errors in forces and moments appear roughly in triplicate, as is expected for these data given a linear model. The forces are recovered nearly perfectly, with normalized errors within order 10^{-14}. The recovered moments have much more significant errors, though all fall within a normalized error of ± 2 percent. Normalized errors in recovered moments for the case of zero applied moment, e.g. for points at the center of the plate, are excluded from the plot due to their misleadingly high normalized errors. The absolute errors for these recovered moments are of equivalent magnitude to those at all other load points considered, however, and fall within $\pm 5 \times 10^{-3}$ N/m.

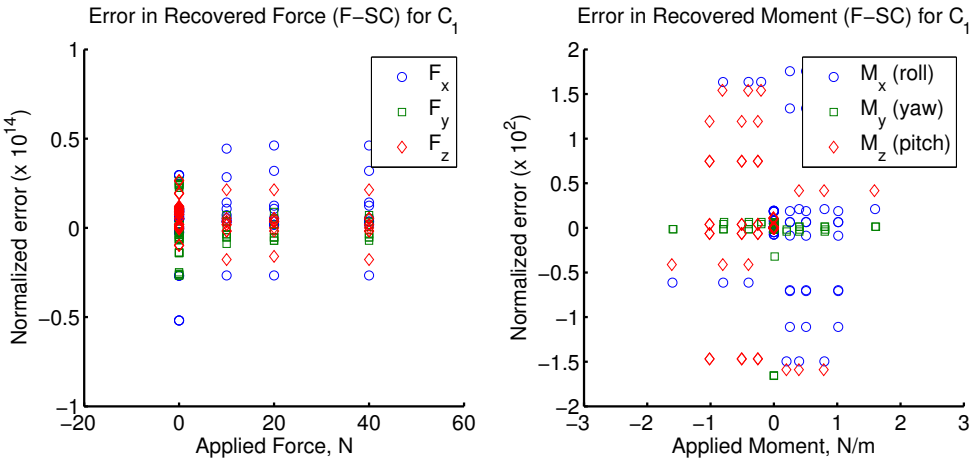

(a) Load case 1

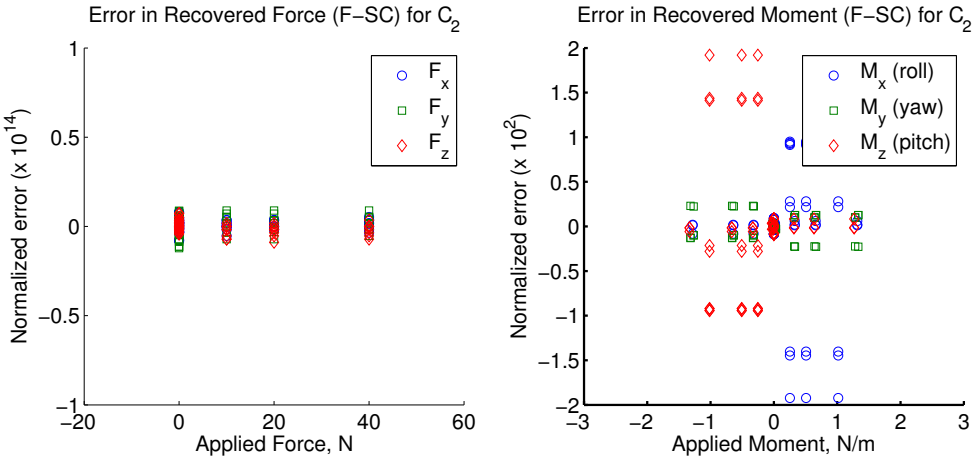

(b) Load case 2

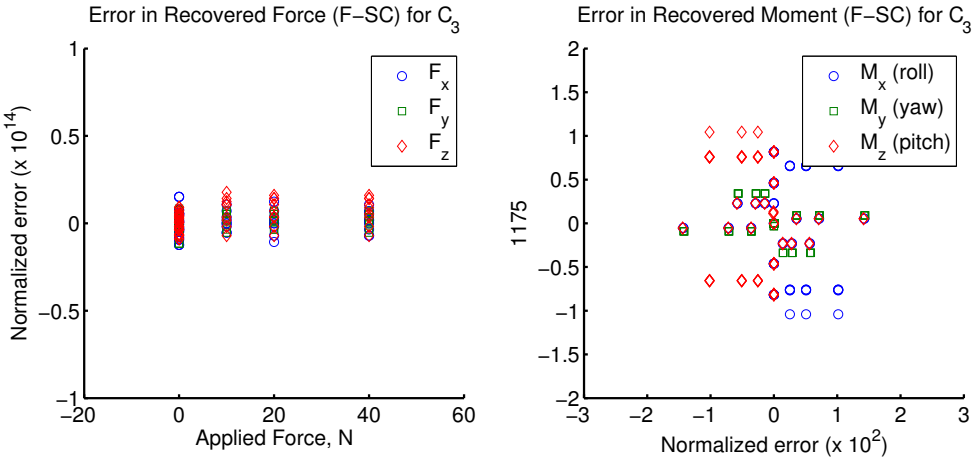

(c) Load case 3

Figure 3.4. Error in recovered forces for each of three loading configurations

A second metric to compare these three load schedules is to attempt recovery of an applied shear load or pressure distributions. Here, the analysis of three pressure distributions, as shown in Figure 3.5, is discussed. These distributions span uniform to 2^{nd} order distributions in spatial coordinates, chosen with the expectation that if simple pressure loads can be recovered, then also superpositions of these pressure distributions should be equally recoverable. We expect load distributions on a test article to be well-approximated as a 2^{nd} order function of the model geometry, so we limit our scope to these three distributions.

For each calibration matrix generated via a loading pattern in Figure 3.3, the sensor output data was used to determine calculated net forces and moments on the plate. The corresponding normalized errors in the resulting calculated forces and moments are plotted against the magnitude of applied load in Figure 3.6.

From these results, we see comparably good recovery of the three pressure distributions for each of the calibration matrices previously defined. The applied forces are recovered with normalized errors below 5×10^{-4} in all three cases, with larger errors present for increasingly asymmetric load distributions. Once again, for the case of zero moment, as in the uniform pressure case for a symmetric model, plots of normalized data are omitted as these errors are visually misleading. For this uniform distribution, the normalized errors in recovered forces are on the order of 10^{-7}, which is substantially lower than those for nonuniform distributions. The largest errors in force recovery come from the quadratic distribution, amounting to just under a tenth of a percent. Of the three load cases, however, there is not a clear best calibration load arrangement. Since the total applied force and moment

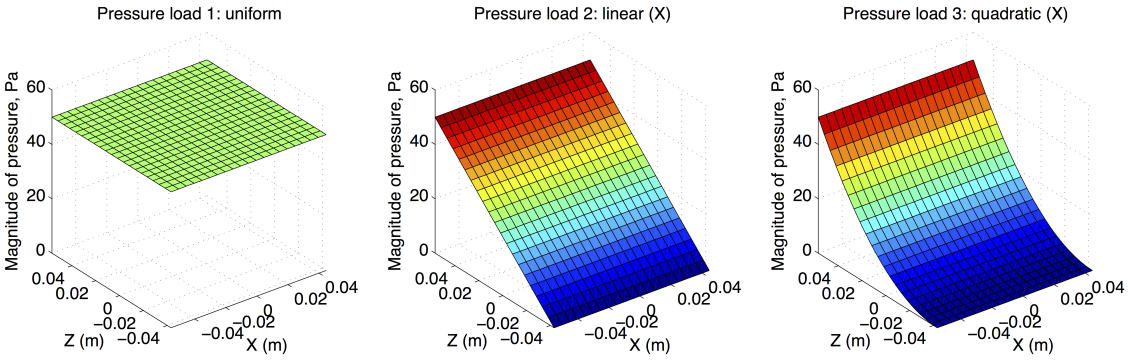

Figure 3.5. Pressure distributions applied to 2-plate model

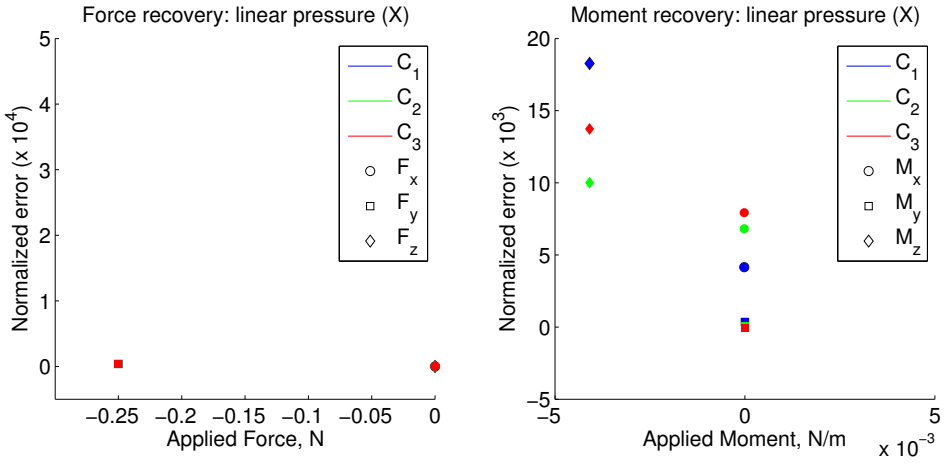

(a) Linear pressure load

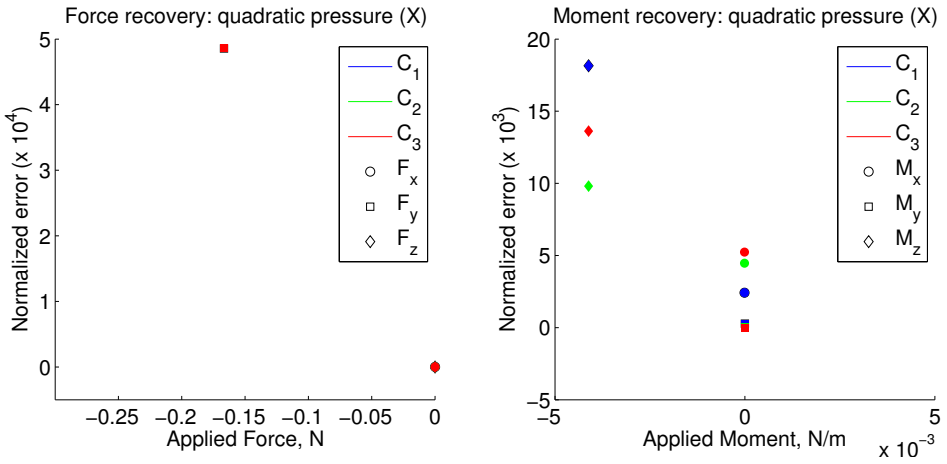

(b) Quadratic pressure load

Figure 3.6. Normalized errors in recovered pressure loads for each of three load cases

can be reasonably recovered from each of these distributions, it suggests that any superposition of these 0^{th}, 1^{st}, and 2^{nd} order pressure distributions is also recoverable to similar accuracy.

3.3.2 Plate Thickness

Practically, the plate thickness represents a measure of how far away from the load surface we can put our force sensors without compromising accuracy. As the plate thickness is increased, however, we also expect a corresponding increase in bending stiffness proportional to the cube of the thickness as the moment of inertia increases. To examine a potential trend as a function of plate thickness, models with five different plate thicknesses ranging from 0.25" - 2", or 6.35 mm to 50.8 mm, shown in Figure 3.7, were created and tested. For each model, an identical pattern of nine load points was created on the top plate surface, and 27 load cases were generated by applying 40N single-component loads at each location in each of three coordinate directions. The number of loads was reduced from the 81 loads previously used, because the linearity of the model has been clearly demonstrated. The load pattern approximately matches load case 2 in Figure 3.3 above, a uniformly distributed square pattern. A calibration matrix was made for each model, and once again the errors in recovered loads can be compared. To visualize a trend as a function of plate thickness, the normalized errors were again computed for each case, and the average of these errors taken for each component, shown in Figure 3.8. What we observe is that the recovered errors in moment are inversely proportional to the cube of the thickness, or equivalently proportional to the bending stiffness of

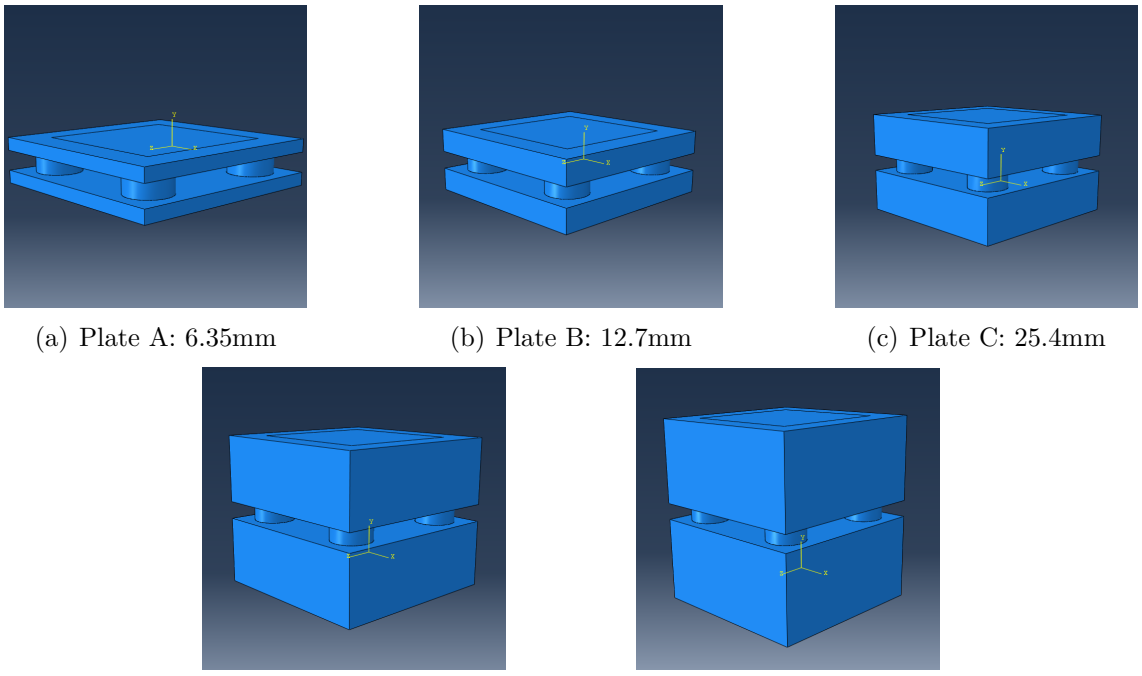

(a) Plate A: 6.35mm (b) Plate B: 12.7mm (c) Plate C: 25.4mm

(d) Plate D: 38.1mm (e) Plate E: 50.8mm

Figure 3.7. Two-plate models with varying thicknesses

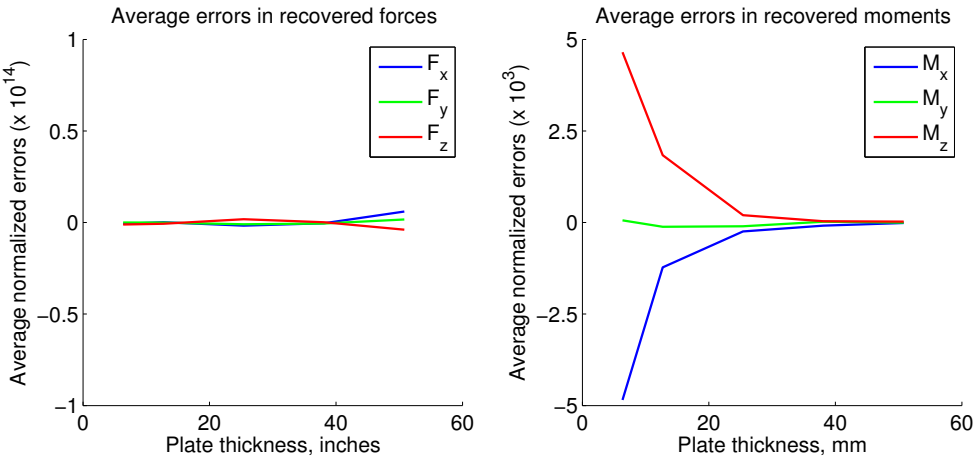

Figure 3.8. Average normalized errors for recovered forces and moments plotted against plate thickness

the plate. This strong correlation therefore suggests that plate thickness has little effect on moment measurement accuracy, and instead the dominant parameter is the plate stiffness.

3.3.3 Plate Modulus

We have already seen that the stiffness of the plate plays a large role in the accuracy of recovered forces and moments as introduced by varying the plate thickness. To isolate the effect of the elastic modulus alone, a model with plate thickness of 25.4 mm was used, using three different material models listed in Table 3.1 to see the effects of the elastic modulus on the calibration matrix. An identical set of load conditions to that in the plate thickness above was used here. We expect that the normalized errors vary linearly with E for a linear relationship between errors and plate stiffness, again as bending stiffness is proportional to EI. As seen in Figure 3.9, as the modulus of the plates is increased, the average error in recovered moment decreases and that in recovered forces increases, though on a much smaller scale. The trend of normalized errors in recovered moments can be fit well to a linear curve, which suggests that relatively large errors in M_x and M_z, or pitch and roll, are primarily due to plate stiffness; errors are inversely proportional to the modulus.

Material	ρ, kg/m^3	E, GPa	ν
Steel (AISI 304)	8000	197	0.29
Titanium (pure)	4500	116	0.34
Aluminum (pure)	2699	68	0.36

Table 3.1. Material properties used for plates

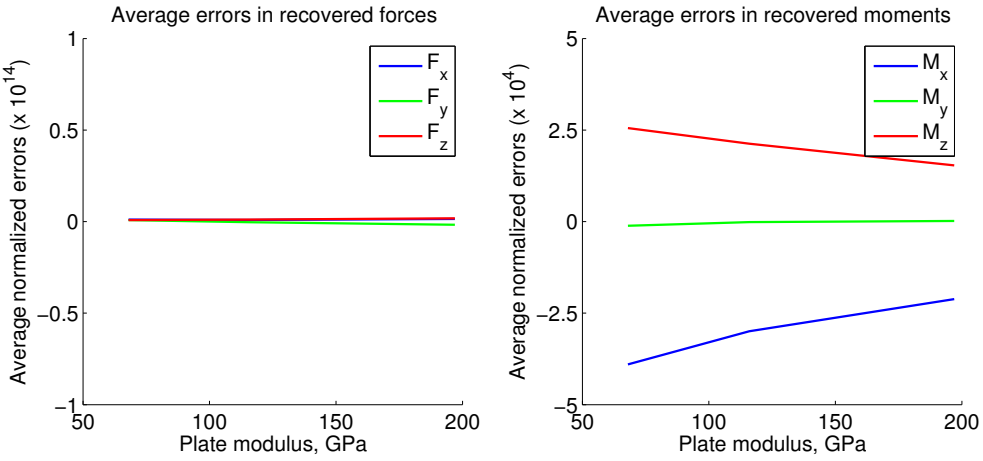

Figure 3.9. Average normalized errors for recovered forces and moments plotted against plate modulus

3.3.4 Sensor Spacing

Finally, several sensor arrangements were examined, each with the same 9-point load case as previously used. A cutaway of the models, excluding the top plate, to visualize the sensor positions is shown in Figure 3.10. Here, we expect that as the sensors are moved closer together, loads applied farther outside the range of the sensors may be more difficult to recover. Very low variation between the arrays can be seen in Figure 3.11. The errors in force and moment for the array with skewed geometry are not plotted due to the nonlinear geometric trend, but the calculated errors do fall linearly between the two symmetric arrangements. The error in recovered forces tends to decrease and the error in recovered moments tends to increase as the sensors are moved toward the outside of the plate, which is consistent with the expected trend.

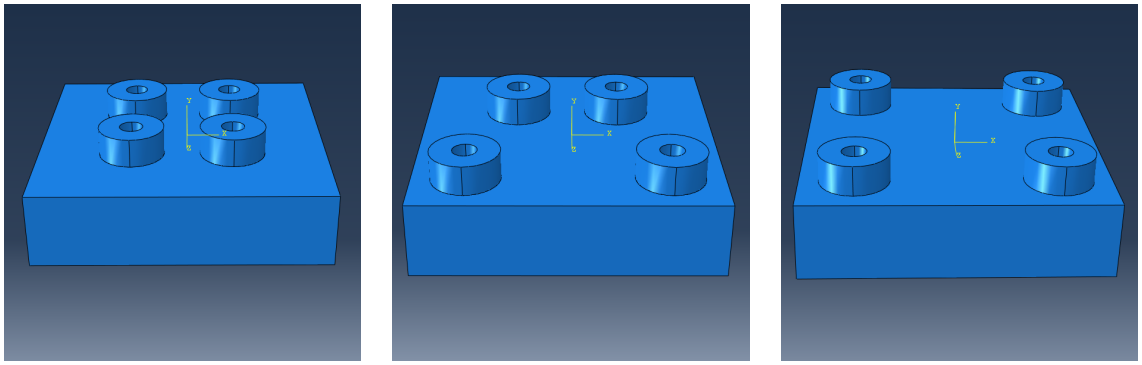

(a) Small spacing (b) Asymmetric arrangement (c) Large spacing

Figure 3.10. Cutaway models with varying sensor spacing

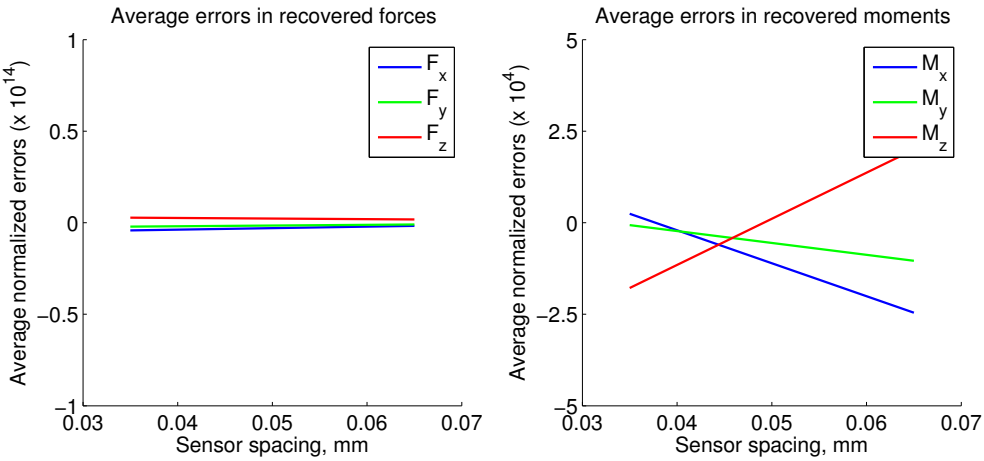

Figure 3.11. Average normalized errors for recovered forces and moments plotted against sensor spacing

3.4 Crosstalk

In addition to looking at the error in recovered loads, these models allow for an analysis of the sensor crosstalk apparent in the calculated sensor data. For the case of perfect sensors, the crosstalk is mitigated in the calibration matrix to a good extent, but it is still preferable to minimize the crosstalk. Crosstalk has several sources including sensor deformation under load or intrinsic material properties such as piezo crystal alignment, however the main contribution to crosstalk comes from reaction forces needed to maintain static equilibrium. For example, a constant

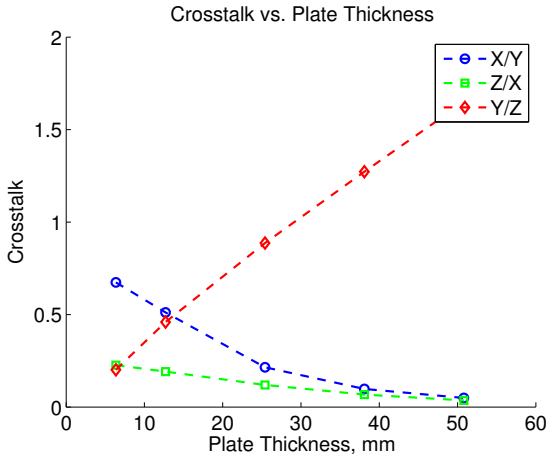

(a) Plate Thickness

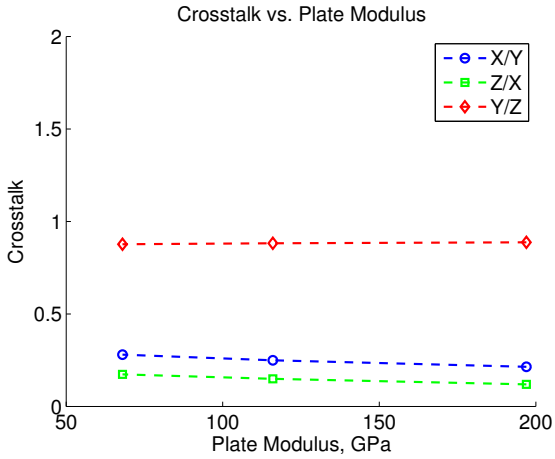

(b) Plate Modulus

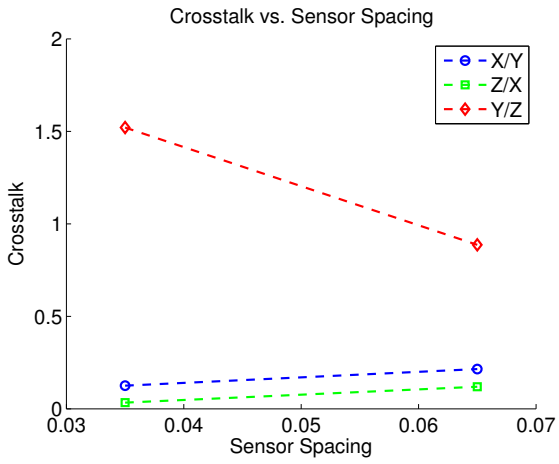

(c) Sensor Spacing

Figure 3.12. Crosstalk as a function of design parameters

shear force (in X or Z) will generate an applied moment about the opposite shear axis, and based on force balance equations can be directly related to the reactions forces, or those forces measured by the sensors. In this case, the plate thickness (e.g. Δy) and sensor spacing (e.g. Δz) are related to those forces measured by each sensor: $\frac{S_y}{S_z} \propto \frac{\Delta y}{\Delta z}$. Therefore as plate thickness is increased and sensor spacing held constant, we expect $\frac{S_y}{S_z}$ to increase, and likewise as plate thickness is held constant and sensor spacing increased, we expect $\frac{S_y}{S_z}$ to decrease. Because the model used here is symmetric in X and Z, three unique measures of crosstalk can be calculated: $\frac{S_x}{S_y}$, $\frac{S_z}{S_x}$, and $\frac{S_y}{S_z}$. Crosstalk values were computed from loads applied at the center of the plate and the corresponding output data. From the results of these analyses in Figure 3.12, it is clear that the overall crosstalk is reduced by decreased plate thickness and a large spacing between sensor elements, as we expect. The modulus of the plate, which affects the degree of sensor deformation, plays a lesser role in the crosstalk as the crosstalk magnitude remains approximately constant.

3.5 Sensor Sensitivity

As design parameters such as plate thickness and sensor spacing are changed, another sensor property is important to consider. Sensitivity of a sensor is a measure of the rate of change of sensor signal output as a function of a changing input, here, applied load. To determine how the sensitivity is affected by the physical design parameters considered in the sensitivity analyses above, the sensitivity of each of the four sensors must be calculated for each design. Loads of magnitudes 10N, 20N, and 30N were applied along each coordinate axis at each of the nine points in the

load array to supplement those 40N loads already applied, for a total of 27 loads per load magnitude. The sensitivity was then calculated as the slope of the raw sensor output as a function of the applied load. For the base design, including steel plates of 25.4 mm thickness and maximum sensor spacing of 65 mm, the sensitivity in all directions can be bounded by approximately 20% given an applied load at the center of the top plate. This means that for an increase of 1N in an applied load, a 20% increase in sensor output is expected. For load points at the corners of the array, the sensors have higher sensitivities, closer to 50%, for this same base design.

In examining trends across the design parameters considered in previous sections, we find that the sensor sensitivity in both axial and shear is increased by decreasing the piezo force sensor spacing, and the axial sensitivity is increased by increasing the plate thickness. These trends indicate an increase in sensitivity of 0.5% per millimeter of decreased sensor spacing, and an increase of axial sensitivity of 1% per mm of increased thickness. There is no apparent dependence of axial or shear sensitivity on plate modulus, and no dependence of shear sensitivity on plate thickness. However, the overall trends suggest that the same parameters that give increased sensor sensitivity align with those parameters that give decreased errors in recovered moments.

3.6 Sensor Error Propagation

Up to this point the sensor elements have been modeled as ideal sensors, in that they fully recover any applied load, as the boundary conditions between the sensors and the plates are kept fully constrained. However, in a laboratory setting,

this is not necessarily the case; there will be some error in the sensor measurements. For each of the sensitivity analyses presented above, a gaussian-distributed error was applied, set so that a two standard deviation range spans values at ±2% of the true value, and the initial calibration matrix is used to recover the original loads. This perturbation has a significant effect on both the recovered force as well as the recovered moment, though again there appears to be very little correlation between these errors and those design parameters considered. Approximate bounds can be given for both the force and moment errors; a conservative bound puts the average normalized error in recovery at 0.4%, and that for moment recovery at 4%. For smaller perturbations in sensor data, such as a 1% and 0.5% errors, a linear trend appears; the normalized error in recovered forces is approximately 20% of the applied perturbation, and that for recovered moments approximately 200% of the applied perturbation.

3.7 Test Article

The final component of the static calibration studies completed thus far is to expand this methodology to a model of our full test article. This model, shown in Figure 3.13, includes a detailed model of the test article and is mounted on a 1 meter sting of diameter 12.7 mm that is fixed to a wall, a simplification of the true sting assembly. The four piezoelectric force sensor discs are mounted below the strain gauge balance assembly, and this covered by a rectangular enclosure. The machined test article is made entirely of stainless steel, including a dummy strain gauge balance which can be swapped out for a real strain gauge balance to assess any

difficulties in integrating these two hardwares. Over 70 threaded holes are machined into all sides of the test article to facilitate many combinations of calibration loads. For the computational model, the majority of the model is meshed using quadratic tetrahedral (C3D10) elements. The toroidal sensor elements are meshed as quadratic prism (C3D15) elements so that nodal forces accurately represent the free-body forces on each surface of the sensor disks.

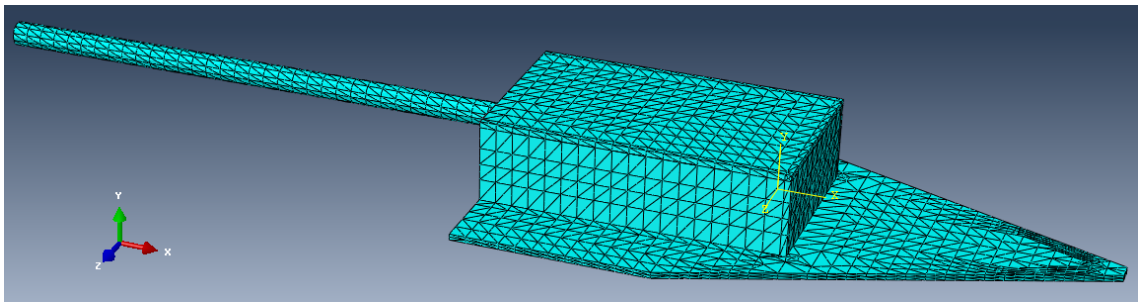

(a) Front view

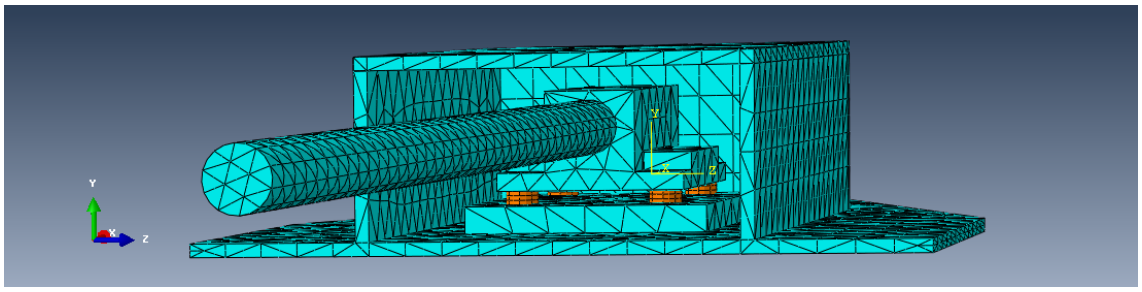

(b) Rear view

Figure 3.13. Two views of mesh of modeled prototype test article with sensors marked in orange

As with the previous analyses on a simplified model, a square matrix of points was defined on the upper rectangular plate of the full prototype test article, as shown in Figure 3.14 and loads from those nine points used to generate a calibration matrix. The applied forces and moments were then recovered using the sensor data from those points, and normalized errors calculated as in Figure 3.15. For

this load array, the normalized moment errors have magnitudes less than 10^{-3}, as compared to 2×10^{-2} for both the simplified models tested previously, showing excellent correlation.

For a more complete analysis on the full test article, we look instead at a load schedule comprised of points on the base calibration plate. The full model was meshed so that the calibration points on the test article correspond to nodes on the finite element model, and the 47 points located on the base plate shown in Figure 3.16. Measured sensor loads were collected for three loads at each node, 40N point loads oriented along each coordinate direction, for a total of 141 load cases. Initially, a calibration matrix was determined using all 141 load cases, and errors calculated for attempted recovery of all input loads. Errors were found to be consistent with those applied on the top surface of the test article. This setup can easily be extended to determine an optimum number and position of calibration load points for recovery of a variety of load scenarios.

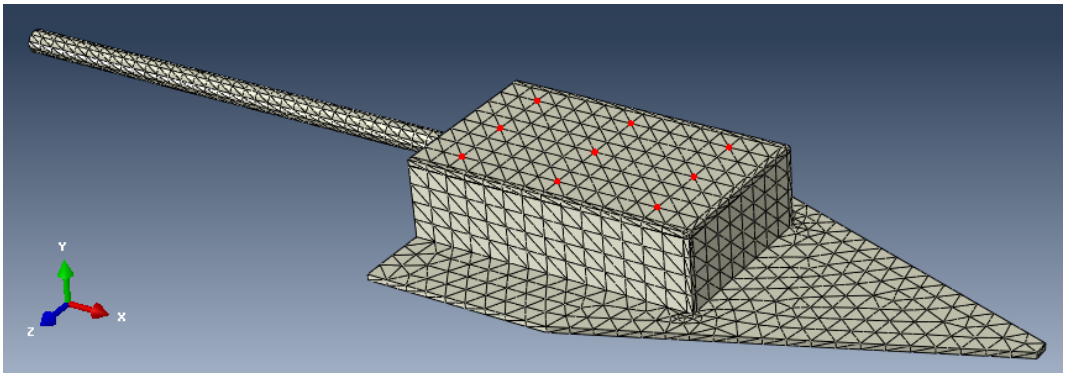

Figure 3.14. Load locations for static calibration on full test article model

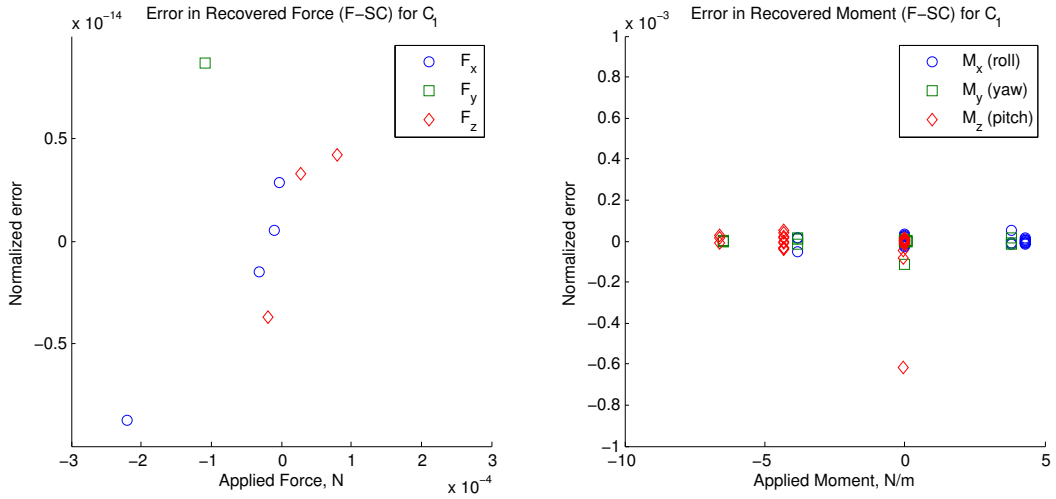

Figure 3.15. Normalized errors for preliminary 27-load static calibration done on full model

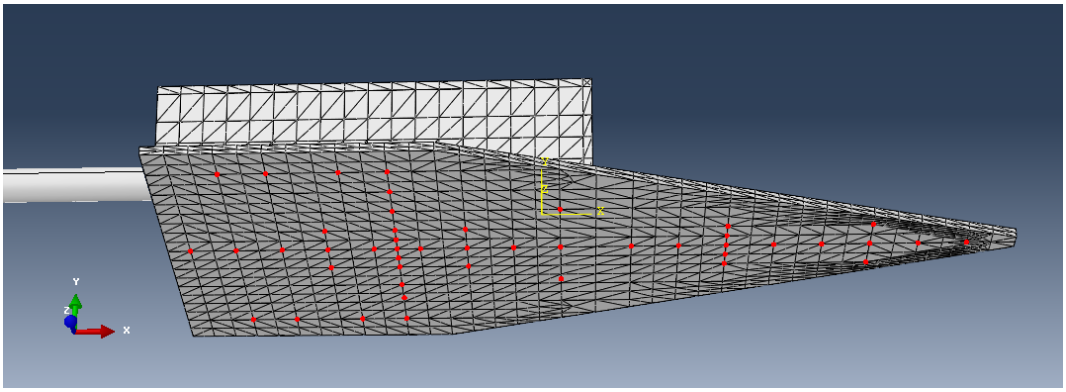

Figure 3.16. Schematic showing all 47 possible calibration points on the base plate of test article

3.8 Conclusions

What this calibration study illuminates is the importance of both design parameters and optimization criteria on force balance design. We would like to minimize both the error in recovered forces and moments as much as possible for as wide a range of load cases as possible, but there are clear tradeoffs to consider. Primarily, high sensor crosstalk can be detrimental to the accuracy of force measurements, and therefore should be minimized if possible - however the same design criteria that tend to minimize crosstalk also are those that decrease the accuracy in moment measurements. Preliminary analysis suggests that the designs that fall in the middle of the ranges considered here are therefore ideal to not have significant crosstalk or errors in moment measurements. Extending the static calibration analysis to the custom test article, see that the methodology developed holds for the test article, with only minor deviations due to the reduced symmetry as compared to the initial simplified model.

Chapter 4: Dynamic Calibration: Preliminary Study

The next step towards improving the fidelity of the model that is being developed is to introduce dynamic calibration. Here, the objective is to recover not only static loads but transient loads. Over a short measurement window, for hypersonic ground testing up to half a second, there is too much signal noise from inertial loading to use a quasistatic approximation in measuring transient loads so acceleration data is used to mitigate these deflections. The dynamic calibration method discussed here is in the time domain, and thus generates a time-dependent calibration matrix useful for sensitivity studies.

4.1 Dynamic Calibration in the Time Domain

For the recovery of transient loads, a time-dependent calibration to correlate N_S components of force sensor data, N_A components of accelerometer data, and N_C components of applied loads can be constructed. For each of the N load cases included in the calibration process, these loads can be separated into steady-state and time-dependent terms, as in Equation 4.1, corresponding to static forces recovered via model-specific static calibration matrix C ($N_S \times N_C$ elements), and dynamic terms to be recovered via dynamic calibration matrix $\hat{C}$ ($N_A \times N_C$ elements). Re-

arranging these terms, we find that the dynamic calibration coefficient matrix can be calculated as in Equation 4.2 at each timestep.

$$F = S_F C + S_A \hat{C} \tag{4.1}$$

$$\hat{C} = \left(S_A^T S_A\right)^{-1} S_A^T \left(F - S_F C\right) \tag{4.2}$$

Note that while the static calibration matrix C is unitless, the dynamic calibration matrix $\hat{C}$ has units of mass as it relates input force data to acceleration data. This implies for our system that since we cannot place accelerometers at the same positions as force sensors, we have created an effective mass matrix that is determined from a different set of nodes than the stiffness matrix. Therefore not only do the positions of the piezo force sensors have an effect on the calibration process, so too do the positions of the accelerometers. In the present analysis, however, we focus on the effect of accelerometer placement over the effect of force sensor placement on the accuracy of dynamic calibration. Here, we have two goals: first, recovery of transient loading given an accurate model of the input load profile, and second, the robustness of this calibration method is tested by in turn reducing the number of accelerometer components available and reducing the time-dependent calibration matrix to a lower-resolution stepwise defined matrix to stay truer to laboratory capabilities.

4.1.1 Simplified Computational Model

The simplified model used for dynamic calibration studies, shown in Figure 4.1, is a modification of the two-plate model used for the static calibration studies: a

fully constrained sting of length 500 mm and diameter 25.4 mm has been affixed at the center of the bottom plate. This model consists of approximately 5500 elements, the majority of which are quadratic tetrahedral (C3D10) elements. The remaining elements, corresponding to the piezo sensor elements, are quadratic wedge (C3D15) elements so that nodal force data may be accurately extracted from the model.

Drawing on the results of static calibration analysis in Chapter 3, a square array of nodes on the surface of the top plate was initially chosen for both the static and dynamic calibration load schedules on this new model. This array of points, denoted C_1, is illustrated in Figure 4.1(b). At a separation distance of 33 mm, these nodes span an area that is nearly equal to that which defines the toroidal force sensor elements, whose centers are at a spacing of 65 mm. During transient loading tests, as with the static loading tests, three-component nodal force data was extracted from the top surface of each force sensor. Additionally, accelerometers were modeled as nodes on the surface of the plates, and three-component acceleration data collected at each of these points.

To proceed with dynamic calibration using the simplified plate model shown in Figure 4.1, first a static calibration matrix was determined as in Equation 3.2. Static loads of 40 N each were applied in each of three coordinate directions at every point in the load array, for a total of 27 individual load cases. The calculated errors between the applied calibration loads and those determined from the measured sensor outputs, again normalized by the euclidean norm of applied force or moment vector, are shown in Figure 4.2. Here we see that the normalized errors in recovered forces are within 10^{-14}, and the normalized errors in recovered moments within

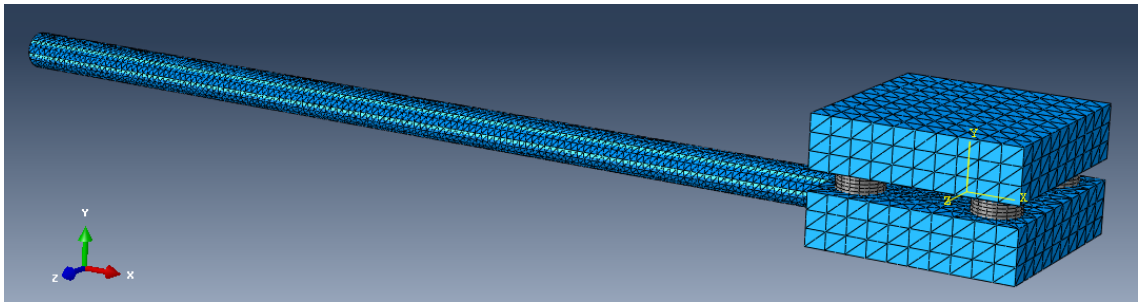

(a) Mesh of simplified 2-plate geometry for dynamic calibration; sensor elements highlighted in orange

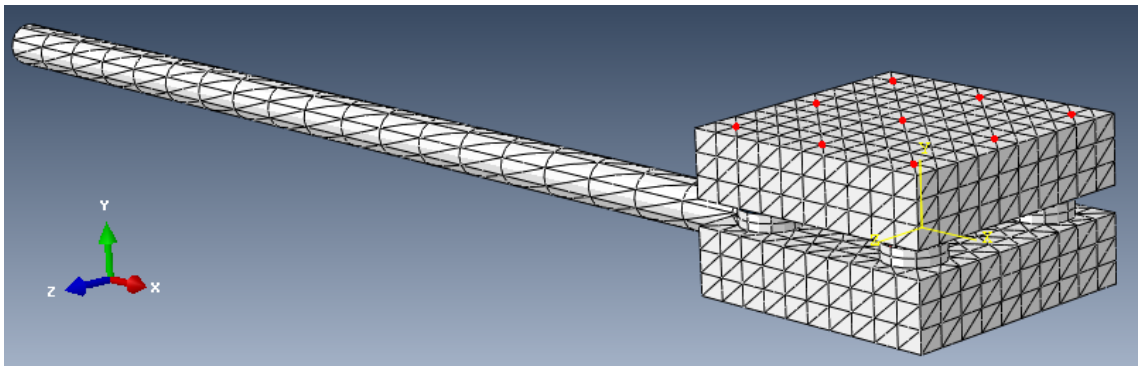

(b) Load locations for static and dynamic calibration marked in red

Figure 4.1. Simplified two-plate model for time-domain dynamic calibration studies

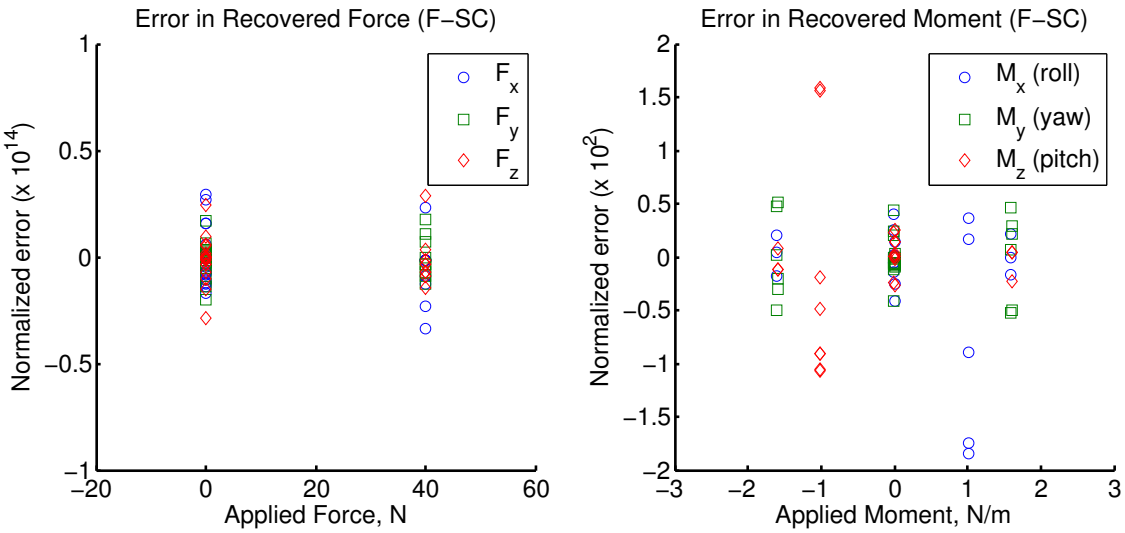

Figure 4.2. Normalized errors in recovered forces and moments from static calibration done on 2-plate model with sting

2×10^{-2}. Comparing these errors to those calculated for a similar load arrangement on the model used for static calibration, seen in Figure, 3.4(b), we see that both sets of errors fall within the same range for both forces and moments. This correlation provides good similarity between models, despite the shift in boundary conditions.

Following the static calibration procedure, dynamic calibration can be completed. In this case, transient step loads of magnitude 40 N were applied at each calibration point in the array described above in each of three coordinate directions, again producing a total of 27 individual loads. Initially, 8 accelerometer locations were chosen at each exterior corner of the model, as shown in Figure 4.5(a). For the duration of the transient load, force and acceleration data were collected from the model at each timestep.

Via the expression in Equation 4.2 above, a linear least-squares analysis was carried out to generate a dynamic calibration matrix at each timestep of the analysis. This calibration was then used to recover input force data for these same points, using the calculated sensor data as in Equation 4.1. Similar to the static loads, the errors in recovered forces and moments are defined as the difference between the assumed applied load and the calculated forces. Again for normalization, the resulting errors are scaled by the euclidean norm of the applied force or moment vector. These calculations are done independently at each time step for each load. The time-dependent calibration procedure was used to recover loads at various timesteps, as well as with varying accelerometer locations, with results shown in the following sections.

4.1.2 Sampling Rate

Computationally, there is a significant tradeoff between the improved resolution of a smaller timestep and the computation time that this resolution requires. We can estimate a lower bound on the sampling rate required for accurate recovery of loads by examining the structural modes of the model; if the sampling rate is too low then even the base frequency will not be included. An eigenvalue analysis of this two-plate model with sting yields the first three natural frequencies of this model: 11.6 Hz, 101 Hz, and 152 Hz are the first bending mode, first torsion mode, and second bending mode respectively. To capture features of each of these three modeshapes, we would like to sample the output at a frequency at least double that of the mode shape. This indicates that for timesteps greater than $\Delta t = 5 \times 10^{-2}$, we will not be able to recover even the first mode, and to recover the first three modes a timestep of at least $\Delta t = 3 \times 10^{-3}$ is required. Based on these values, we investigate the accuracy of this dynamic calibration methodology based on the number of modes measured.

To examine this trend, force and acceleration data were sampled at timesteps of 10^{-2} s, 10^{-3} s, and 10^{-4} s, each with identical load locations and accelerometer locations. Here, 8 accelerometers are positioned at the exterior corners of both the top and bottom plates. As an example, force and moment components of an applied step load along the normal (Y) axis at the center of the upper plate are plotted in Figure 4.3 and 4.4, respectively. These plots show the applied step load, the measured load on the sensors, and the calculated resultant load profile using the

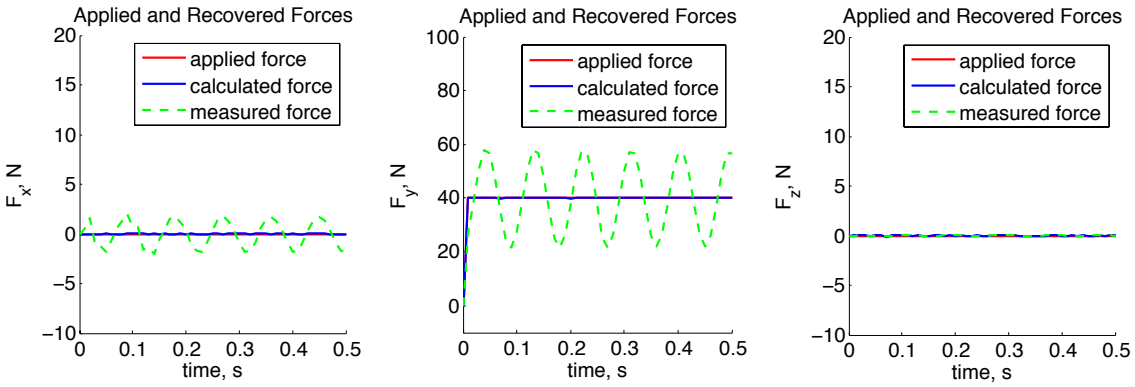

(a) F_x, $\Delta t = 10^{-2}$s

(b) F_y, $\Delta t = 10^{-2}$s

(c) F_z, $\Delta t = 10^{-2}$s

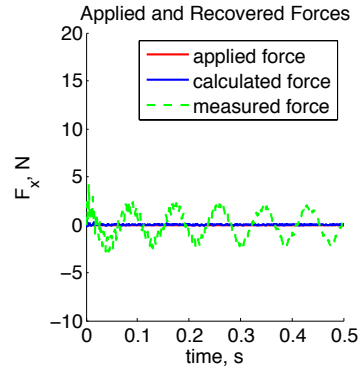

(d) F_x, $\Delta t = 10^{-3}$s

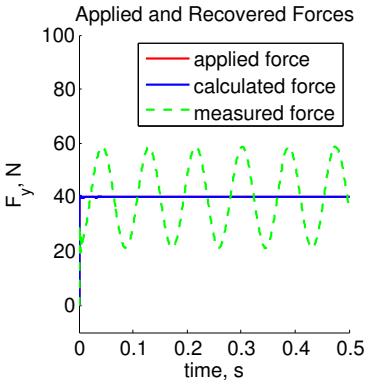

(e) F_y, $\Delta t = 10^{-3}$s

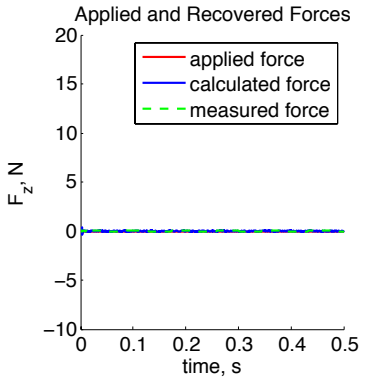

(f) F_z, $\Delta t = 10^{-3}$s

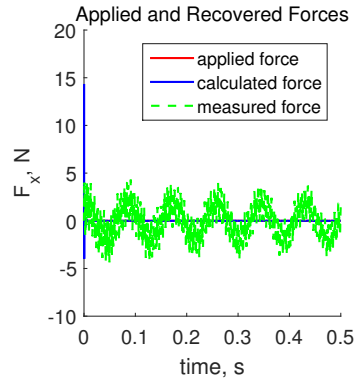

(g) F_x, $\Delta t = 10^{-4}$s

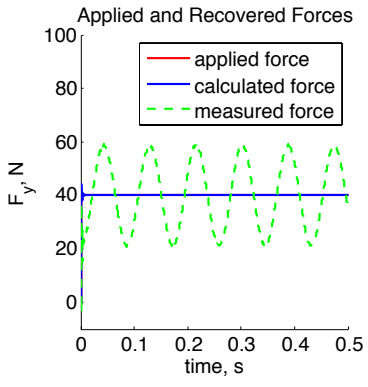

(h) F_y, $\Delta t = 10^{-4}$s

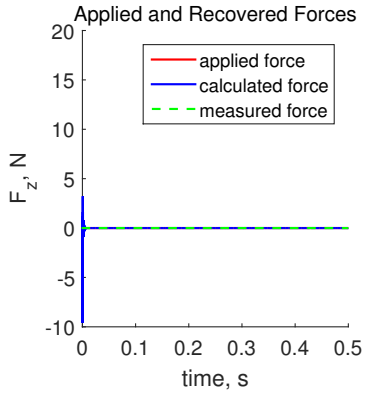

(i) F_z, $\Delta t = 10^{-4}$s

Figure 4.3. Applied and recovered force profiles for step load applied at center of plate for increasing sampling rate, where measured force is the observed force profile without dynamic compensation, and calculated force is after dynamic compensation. Note that the vertical scale for each component shown differs to show detail.

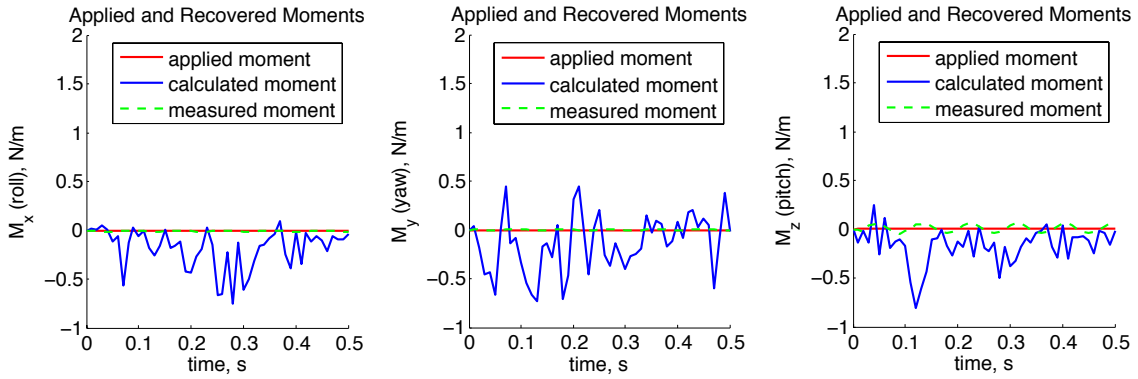

(a) M_x, $\Delta t = 10^{-2}$s (b) M_y, $\Delta t = 10^{-2}$s (c) M_z, $\Delta t = 10^{-2}$s

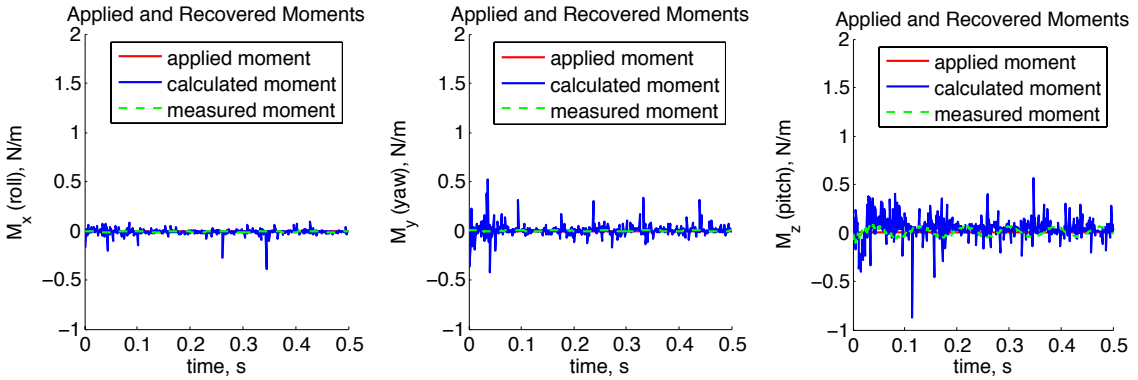

(d) M_x, $\Delta t = 10^{-3}$s (e) M_y, $\Delta t = 10^{-3}$s (f) M_z, $\Delta t = 10^{-3}$s

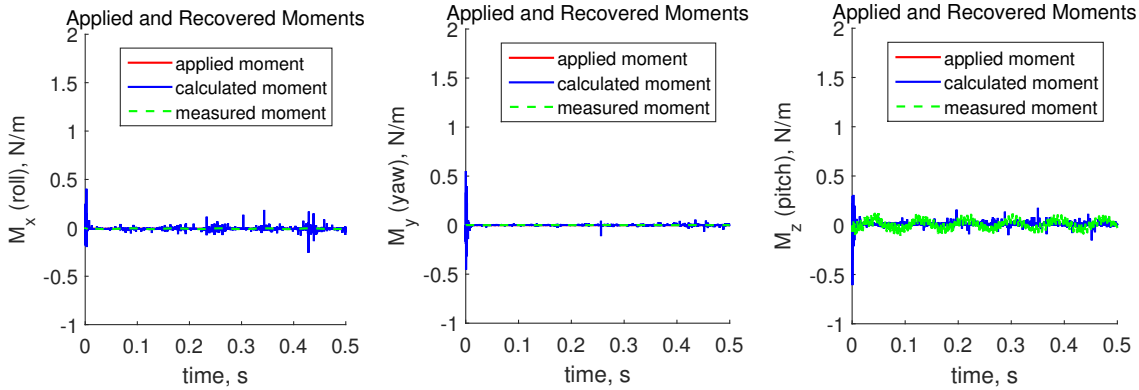

(g) M_x, $\Delta t = 10^{-4}$s (h) M_y, $\Delta t = 10^{-4}$s (i) M_z, $\Delta t = 10^{-4}$s

Figure 4.4. Applied and recovered moment profiles for step load applied at center of plate for increasing sampling rate, where measured moments are observed profiles without dynamic compensation, and calculated moments are obtained after dynamic compensation.

time-dependent calibration matrix for each sampling rate considered.

The lowest sampling rate, $\Delta t = 10^{-2}$ s, by the above reasoning should include at most the first mode, and we see generally poor recovery of applied loads, particularly the moments which show an average error of approximately 2×10^{-1} N/m. In contrast, the mid-range sampling rate, $\Delta t = 10^{-3}$ s, should include all of the first three modes, and has a lower average absolute error in recovered moments, at approximately 5×10^{-2} N/m. Decreasing the timestep further to $\Delta t = 10^{-4}$ s shows again increased ability to recover moment profiles, with average absolute errors of 2×10^{-3} N/m. The absolute error in recovered forces for these three cases, meanwhile, remains roughly constant, within approximately 5×10^{-3} N for all components, or a 0.01% error given an applied 40N load.

From these data, it is clear that higher sampling rates, thereby allowing measurement of higher modes, are essential to improved accuracy in recovered loads. However, there remains a tradeoff between accuracy and computation time, as reducing the timestep requires an order of magnitude increase in computation time. Therefore for this simplified two-plate model, we use a timestep of $\Delta t = 10^{-3}$ for future analyses. For a more complex model where natural frequencies may be closer together, a higher timestep may be usefully employed as these data do provide more accurate data, but at a higher computational cost.

4.1.3 Accelerometer Locations

The addition of acceleration measurements for the purpose of dynamic calibration introduces additional degrees of freedom when optimizing sensor placement.

Here we keep the location of piezo force sensors fixed at a separation distance of 65 mm, but vary the location of accelerometers to assess any resultant effect. The three arrangements considered are shown in Figure 4.5: exterior corners of the top and bottom plates, interior corners of top and bottom plates, and a small array, 40 mm on a side, in the center of each of the top and bottom plates. For a sampling frequency of $\Delta t = 10^{-3}$ s and a total duration of 0.2 s, a dynamic calibration matrix was determined for each of these three accelerometer arrays as in previous tests, with the same load schedule of unidirectional step loads applied at every point in the calibration load array depicted in Figure 4.1(b) for a total of 27 load cases. For each dynamic calibration matrix, absolute errors were calculated between the loads applied to generate that same calibration matrix and those loads calculated from the force sensor and accelerometer data.

The average absolute errors in recovered force and moment data are roughly equivalent for each of these three accelerometer arrays: for a 40 N step load applied in Y at the center of the top plate, and sampling from 0.03 seconds onwards, the average absolute errors in recovered forces are within 2×10^{-2} N, 3×10^{-3} N, and 4×10^{-2} N for all components of force for the models depicted in Figure 4.5(a) - (c), respectively. Including the data from 0 to 0.03 seconds, the average absolute errors in recovered forces are approximately 1 N for the latter two accelerometer arrays, in contrast to the results for the case of accelerometers place on the outer exterior corners where the average absolute error in recovered forces is approximately 2×10^{-3} N. The large errors at very small times t are likely due to the limitations of the analysis; application of a step load at time zero is not instantaneous but

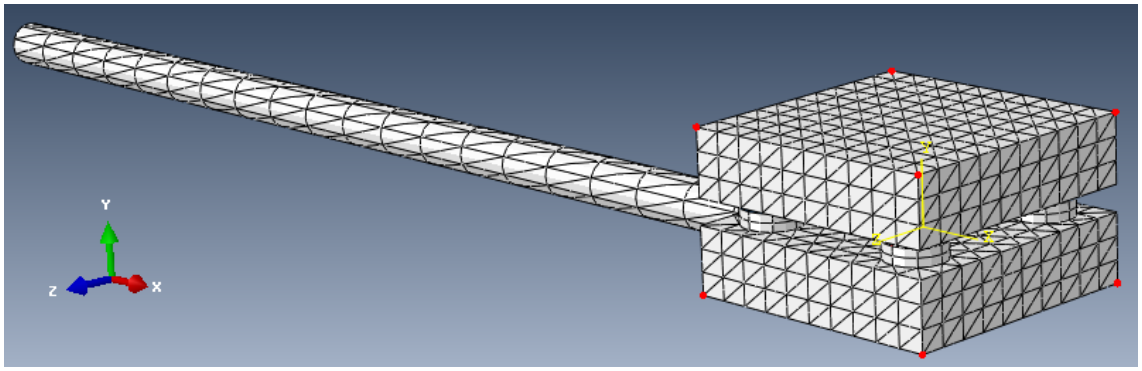

(a) Exterior corners

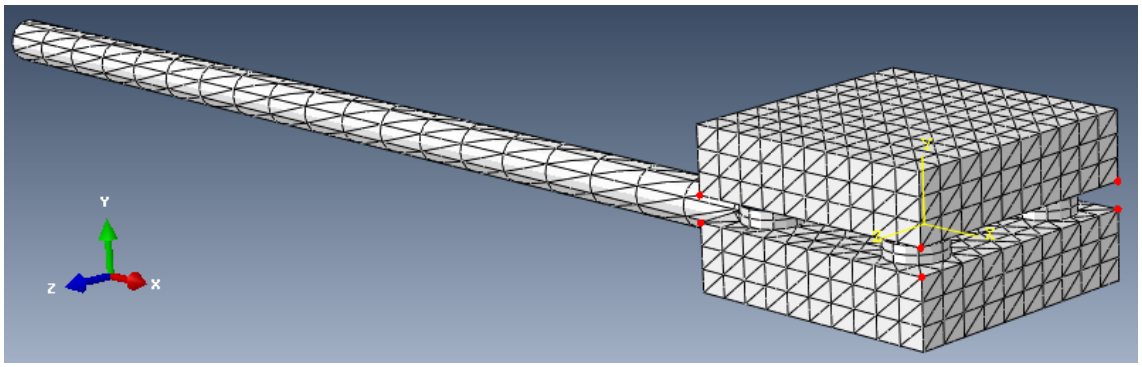

(b) Interior corners

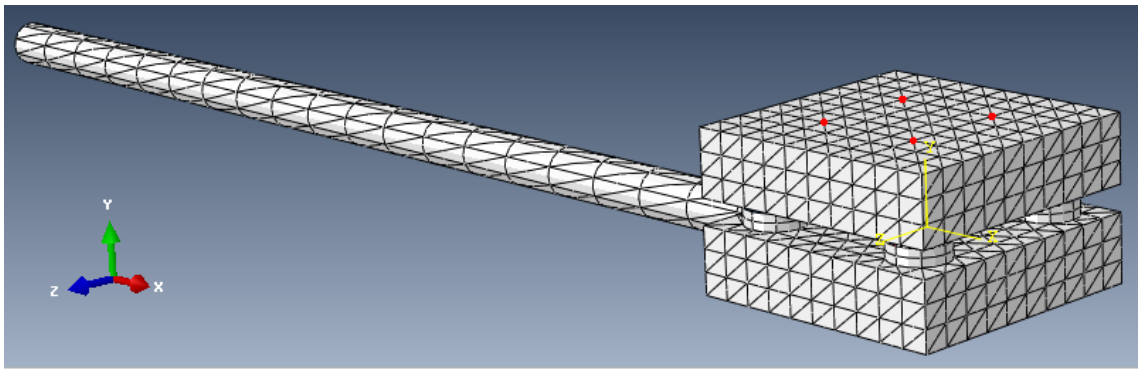

(c) Exterior plate surfaces

Figure 4.5. Accelerometer positions

instead ramped up over the initial timestep in the finite element simulation and therefore the data for very low values of t do not agree with real test conditions of an impulsive load. The results here show that for the accelerometer arrays that are closer to the center of the model, the errors induced by this modeling discrepancy are quite large, and less so for the array with accelerometers in more distant locations. This suggests that placement of accelerometers in more distant locations from the center of the model may provide a better calibration matrix, particularly at early timepoints when strong impulses are expected.

This preliminary analysis of accelerometer arrangements is, however, only an approximation of the laboratory setup – the experimental setup in use includes only 12 uniaxial accelerometers. To match this system more closely, we therefore look at a maximum of 12 components. Some insight into optimal placement of accelerometers is taken from a discussion by Cardou and Angeles [16] where the 9-accelerometer 3-2-2-2 array initially proposed by Padgaonkar et al [17], sketched in Figure 4.6, is characterized. This arrangement of accelerometers allows for estimation of the acceleration at a specific point, i.e. this array is point determined, based on the accelerations at each of the four biaxial or triaxial accelerometer positions and the vectors from these locations to the point of interest. This array is also tangentially determined (allows for estimation of angular accelerations) for the case of a non-coplanar array, but is not generally radially determined (does not allow for estimation of angular velocities). A different array which allows recovery of different acceleration measures may therefore be an avenue for further studies.

To determine the efficacy of this accelerometer array for this simplified two-

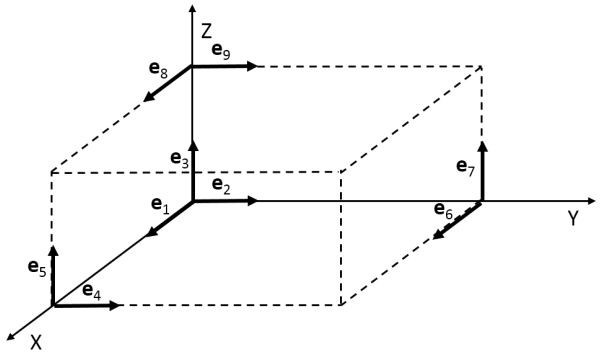

Figure 4.6. Sketch of 3-2-2-2 accelerometer array proposed by [17]

plate model, we look at the system with accelerometers placed at the exterior corners of the top and bottom plates as shown in Figure 4.5(a). From this model, we can extract only the 9 acceleration elements that match the 3-2-2-2 array, and again generate a dynamic calibration matrix from this data. From here we compare the absolute errors in the recovered input force and moment loads to that for a calibration matrix generated from the full set of 24 acceleration elements collected. The input, measured, and calculated loads are plotted for both cases in Figure 4.7 for a sample point at the center of the plate. By comparison of the resulting force and moment data for both accelerometer arrays, there is very little loss of information by reducing the number of acceleration components in the system. This implies that the results using 24 uniaxial accelerometers (three-component data collected at each exterior corner of the two-plate array) gives sufficiently redundant data that the accuracy of recovered forces and moments is not significantly improved over the result using 9 uniaxial accelerometers as in the 3-2-2-2 array. This result also agrees with the assertion that this 3-2-2-2 arrangement of accelerometers can accurately estimate an acceleration profile for a highly symmetric model, and also

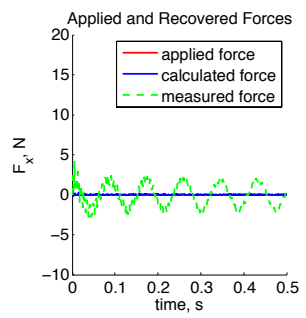

(a) F_x, 24 accelerometers

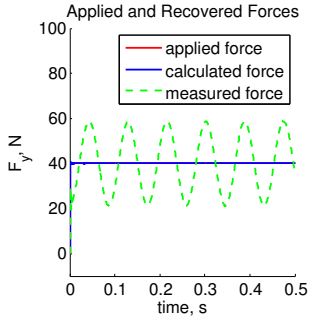

(b) F_y, 24 accelerometers

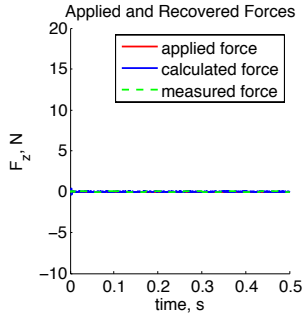

(c) F_z, 24 accelerometers

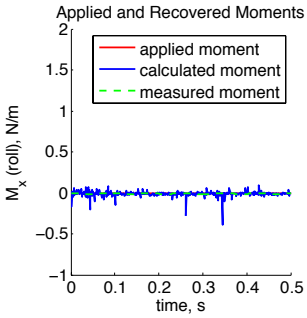

(d) M_x, 24 accelerometers

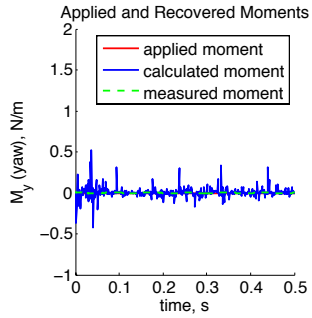

(e) M_y, 24 accelerometers

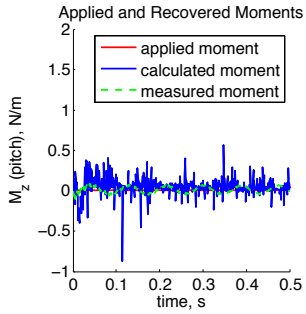

(f) M_z, 24 accelerometers

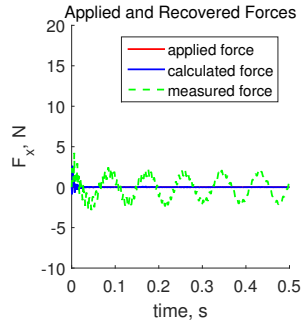

(g) F_x, 9 accelerometers

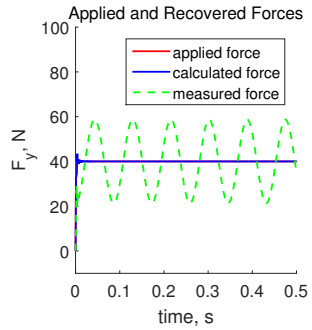

(h) F_y, 9 accelerometers

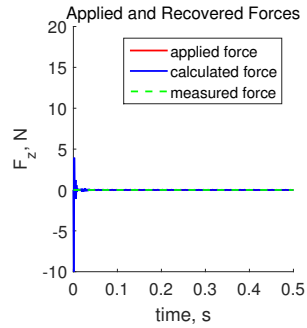

(i) F_z, 9 accelerometers

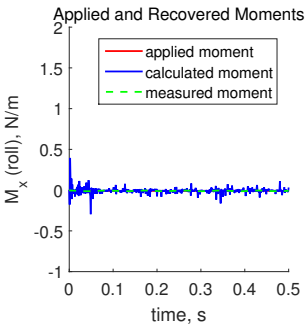

(j) M_x, 9 accelerometers

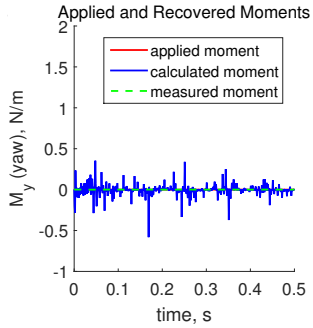

(k) M_y, 9 accelerometers

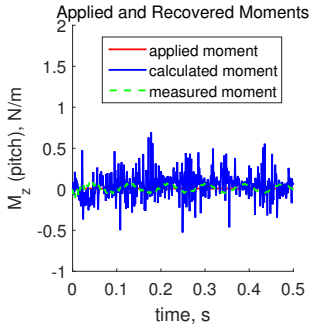

(l) M_z, 9 accelerometers

Figure 4.7. Recovered forces and moments for applied step load at the center of top plate using two accelerometer arrays. These plots show both measured (uncompensated) forces and moments, as well as the calculated (with compensation) forces and moments.

gives an allowance of three sensors in our experimental setup to account for the less symmetric shape of the full test article.

4.1.4 Stepwise-Defined Calibration Matrix

The time-dependent calibration matrix as defined in Section 4.1 is relatively computationally intensive, particularly as timesteps decrease, because the elements in this matrix are calculated at every timestep. Therefore it is instrumental to attempt to reduce this matrix to a much simpler expression that can recover applied loads and continue to reasonably mitigate inertial loads. A first attempt was carried out by dividing the 0.5 second interval over which data were collected evenly into five segments, and a reduced matrix defined stepwise by taking the value of the calibration matrix at the final timepoint in each segment. In this reduced calibration matrix, the first 0.1 seconds of data are recovered using the calibration matrix calculated from instantaneous sensor output at 0.1 seconds, the next 0.1 seconds of data recovered using the calibration matrix calculated from instantaneous sensor output at 0.2 seconds, and so on. This new stepwise-defined matrix was then used to recover the input transient step load, and those results are plotted in Figure 4.8. The force and moment data can be compared to those loads recovered using the full dynamic calibration matrix that was generated at every timestep, which is the same data as shown in Figures 4.7(a) through 4.7(f). These results show that inertial loads are well compensated and show good correlation to the input data over some intervals, and are incorrectly compensated and show significant deviation over other intervals. See again that data at small times t are poorly recovered using the constant

calibration matrix. This error has several sources, the main effect being that a constant calibration matrix defined in this way is unlikely to be a good fit to most of the data without a careful look at the frequency content of the data. Moreover, there is more variability in the data near $t = 0$ as the computational model does not apply an instantaneous impulsive load but instead ramps to the desired value over the first few time increments of the simulation. These results suggest that continuing with this method requires specific tuning to the natural frequencies of the system to define an appropriate simplification of the full time-dependent calibration matrix to ensure that each frequency that arises from inertial loading is appropriately compensated.

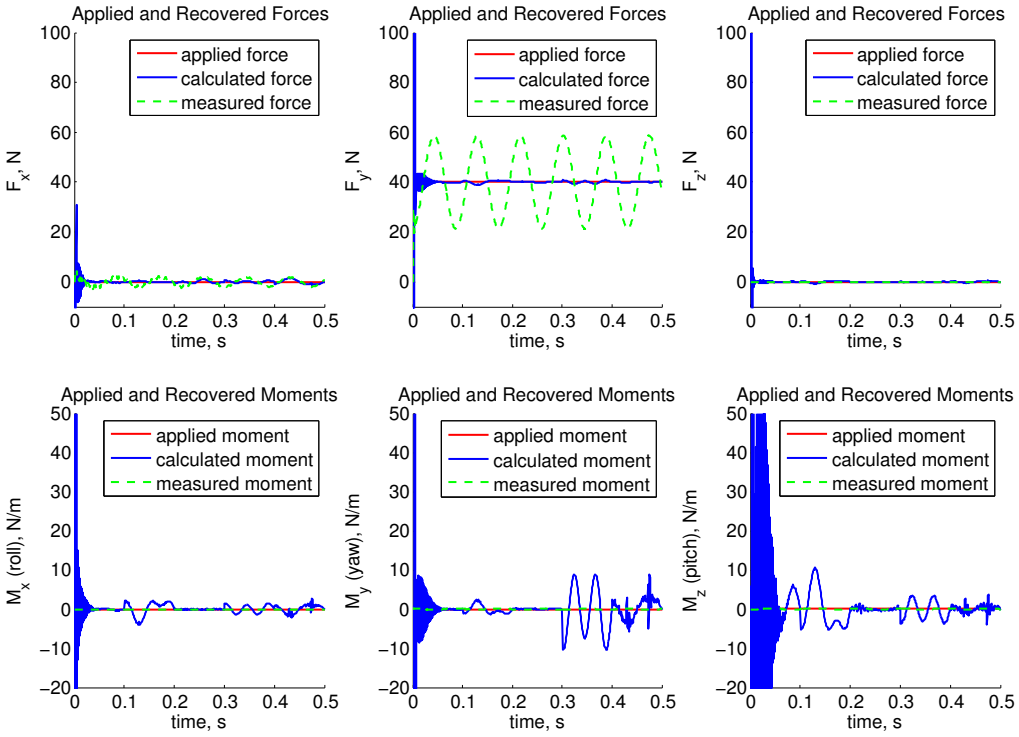

Figure 4.8. Recovered forces and moments for applied step load at the center of top plate using stepwise defined calibration matrix. Plots show both measured forces and moments (without dynamic compensation) and calculated forces and moments (with dynamic compensation).

4.2 Test Article Calibration

Again we can easily extend the analyses herein to the test article. In conjunction with the static calibration matrix determined from this same array of nodes, a dynamic calibration matrix can be determined, and further used to attempt recovery of the input loads. The large set of data provided by the various load locations on the test article allows for further optimization tests to be enacted, notably to determine an optimal number of loads and the locations of those loads for accuracy of both static and dynamic calibration.

4.3 Conclusions

These studies present the difficulties in balancing a computationally intensive calibration process with the accuracy of the system. While design parameters such as accelerometer placement play a role in the accuracy of the calibration process, a much larger component is careful attention to the natural frequencies of the system to choose appropriate sampling rates for accurate load recovery.

Simplifications were made in the analysis presented here to reflect ideality of the computational model, primarily the omission of any significant structural damping. To better match the true system for use in an experimental setting, damping may have to be added to the system, along with any correction for out of phase acceleration profiles. This chapter therefore represents work in progress and provides many avenues for further research.

Chapter 5: Conclusions and Future Work

To summarize this work, first a study of static calibration for use in recovering unknown constant loads on a generic test article was completed, with results showing good agreement between applied loading scenarios and that generated by the calibration procedure. Further, several sensitivity analyses were conducted to assess the effects of geometric properties of the test article on accuracy of the calibration matrix, where the main finding relates sensor crosstalk to accuracy in force and moment measurements: high sensor crosstalk can be detrimental to the accuracy of force measurements, and low sensor crosstalk is correlated to decreased accuracy of moment measurements.

Secondly, an approach to dynamic calibration was investigated, using data collected in the time domain to reconstruct applied force and moment profiles. For this calibration process, a dynamic calibration matrix must be calculated at each timestep and is therefore also time dependent. This method remains preliminary and have challenges moving forward. The time dependent calibration remains a preliminary methodology, as the accuracy of the method depends on the sampling rate of force and acceleration data, and therefore is computationally expensive and inefficient for general use.

There are several additional avenues to further this work, including continued sensitivity analyses, optimization studies, and continued work towards increasing the fidelity of the computational models presented for static and dynamic calibration to better reflect experimental limitations. Finally, experimental work to corroborate the computational tests discussed herein is ongoing, and results from those experiments can continue to be included in the computational model to improve the calibration methodology.

1. These items focus on further sensitivity analyses and optimization to consider:

    - Complete a full analysis of geometric properties, such as plate thickness and force sensor placement, pertaining to the accuracy of dynamic calibration for both the simplified and full model.
    - Consider an optimization study of accelerometer placement in tandem with an optimization study for force sensor placement, and determine which, if any, has a stronger effect on the accuracy of dynamic calibration.

2. These items focus on increasing the fidelity of the computational model to reflect true conditions:

    - Investigate a reliable method to recover unknown transient loads via dynamic calibration for loads that have a different functional form than the calibration loads applied.
    - Model true response of piezoelectric force sensors, including voltage readouts, sensor hysteresis, and signal decay, and incorporate these properties

into computational static and dynamic calibration procedures.

- Consider internal boundaries in test article, particularly preload studs for piezoelectric force sensors and pin connectors for strain gauge balance enclosure.
- Consider the use of nonlinear least squares models for static and dynamic calibration to include any true nonlinear behavior in the sensors.
- Further models for acceleration compensation may be considered to improve the methodology included here, particularly those involving angular velocity measurements, as well as refinement of the methods proposed herein to compensate high-frequency loads more accurately.

References

[1] M. S. Holden, T. P. Wadhams, J. Harvey, and B. J. Walker, "Experimental and Numerical Studies on Hypersonic Vehicle Performance in the LENS Shock and Expansion Tunnels", *AIAA Paper 2006-125*.

[2] S. J. Laurence, J. M. Schramm, S. Karl, and K. Hannemann, "An Experimental Invesigation of Steady and Unsteady Combustion Phenomenon in the HyShot II Combustor", *AIAA Paper 2011-2310*.

[3] S. J. Laurence, H. Ozawa, D. Lieber, J. M. Schramm, and K. Hannemann, "Investigation of Unsteady/Quasi-Steady Scramjet Behavior using High-Speed Visualization Techniques", *AIAA Paper 2012-5913*.

[4] L. Resch, C. Decesaris, and E. Hedlund, "The Naval Surface Warfare Center Hypervelocity Wind Tunnel 9 Hypersonic Shroud Testing Capability", *AIAA Paper 92-0676*.

[5] L. Resch, L. Zentz, and J. Allwine, "Hypersonic Shroud Separation Testing and Modelling Capabilites at the Naval Surface Warfare Center Hypervelocity Wind Tunnel 9", *AIAA Paper 94-2495*.

[6] M. Holden, T. Wadhams, M. MacLean, A. Dufrene, E. Mundy, and E. Marineau, "Review of Basic Research and Development Programs Conducted in the LENS Facilities in Hypersonic Flows", *AIAA Paper 2012-469*.

[7] M. Holden, B. Walker, R. Parker, and R. Bergman, "Experimental Studies of the Effects of Combustion on the Characteristics of Jet Interaction on Interceptor Performance in Supersonic and Hypersonic Flows", *AIAA Paper 99-0808*.

[8] P. A. Gnoffo, S. A. Berry, and J. W. Van Norman, "Uncertainty Assessments of Hypersonic Shock Wave-Turbulent Boundary-Layer Interactions at Compression Corners", *Journal of Spacecraft and Rockets*, vol. 50, no. 1, 2013.

[9] E. C. Marineau, "Force Measurements in Hypervelocity Flows with an Acceleration Compensated Piezoelectric Balance", *Journal of Spacecraft and Rockets*, vol. 48, no. 4, pp. 697-700, 2011.

[10] E. C. Marineau, M. MacLean, E. Mundy, and M. Holden, "Force Measurements in Hypervelocity Flows with an Acceleration Compensated Strain Gauge Balance", *Journal of Spacecraft and Rockets*, vol. 49, no. 3, 2012

[11] V. Storkmann, H. Olivier, and H. Gronig, "Force Measurements in Hypersonic Impulse Facilities" *AIAA Journal* vol. 36, no. 3, p. 342-348, 1998.

[12] J. Schmisseur, "Hypersonics Into the 21st Century: A Perspective on AFOSR-Sponsored Research in Aerothermodynamics" *AIAA Paper 2013-2606*

[13] D. Marren and J. Lafferty. "The AEDC Hypervelocity Wind Tunnel 9", in Advanced Hypersonic Test Facilities, F. Lu and D. Marren, eds. American Institute of Aeronautics and Astronautics, 2002.

[14] G. Gautschi, "Piezoelectric Sensorics", *Springer*, Berlin, Germany, 2002.

[15] A. X. Collopy, E. C. Marineau, and S. W. Lee, "Development of Dynamic Force Measurement Capabilities at AEDC Tunnel 9", *AIAA Paper 2014-0983*

[16] P. Cardou, J. Angeles, "Linear Estimation of the Rigid-Body Acceleration Field From Point-Acceleration Measurements", *Journal of Dynamic Systems, Measurement, and Control*, vol. 131, no. 4, 2009

[17] A. J. Padgaonkar, K. W. Krieger, A. I. King, "Measurement of Angular Acceleration of a Rigid Body Using Linear Accelerometers", *J. Appl. Mech.* vol. 42, no. 3, p. 552-556, 1975.

[18] M. A. Rotea, L. A. Randal, G. Song, and S. P. Schneider, "Model identification of a Kulite pressure transducer", *AIAA Paper 96-2278*.

[19] M. M. Abdel-jawad, D. J. Mee, and R. G. Morgan, "New calibration technique for multiple-component stress wave force balances", *Review of Scientific Instruments*, vol. 48, pp. 065101-1-065101-7, 2007.

Additional Reading

[1] L. Bernstein, "Force Measurements in Short-duration Hypersonic Facilities", *NATO Science and Technology Organization*, AGARD-AG-214, 1975.

[2] G. R. Duryea Jr. and J. F. Martin, "An Improved Piezoelectric Balance for Aerodynamic Force Measurements", *IEEE Transactions on Aerospace and Electronic Systems*, vol. AES-4, no. 3, 1968.

[3] D. D. Joshi, P. Vadassery, and F. K. Lu, "Acceleration Compensation for Drag Measurements in Hypersonic Shock Tunnel", *AIAA Paper 2013-1020*.

[4] D. Landman, D. Yoder, C. Reinholtz, P. Jalbert, and D. Garrard, "A Design of Experiments Approach Applied to Wind Tunnel Balance Calibration at Arnold Engineering Development Complex", *AIAA Paper 2013-1019*.

[5] Y.-J. Li, J. Zhang, Z.-Y. Jia, M. Qian, "A novel piezoelectric 6-component heavy force/moment sensor for huge heavy-load manipulator's gripper", *Mechanical Systems and Signal Processing*, vol. 23, pp. 1644-1651, 2009.

[6] M. MacLean, A. Dufrene, and M. Holden, "Spherical Capsule Heating in High Enthalpy Carbon Dioxide in LENS-XX Expansion Tunnel", *AIAA Paper 2013-0906*.

[7] D. J. Mee, "Dynamic calibration of force balances for impulse hypersonic facilities", *Shock Waves*, vol. 12, pp. 443-455, 2003.

[8] M. Richardson and B. Schwarz, "Modal Parameter Estimation from Operating Data", *Sound and Vibration*, Jan 2003.

[9] G. Schewe, "Force and Moment Measurements in Aerodynamics and Aeroelasticity Using Piezoelectric Transducers", *Springer Handbook of Experimental*

Fluid Mechanics, Special Print 920-363e-03.08, Springer-Verlag Berlin Heidelberg, 2007.

[10] G. J. Smolinski, "Proof of Concept for Testing Acceleration Compensation Force Balance Techniques in Short Duration Flows with a CEV Capsule", *AIAA Paper 2007-1010*.

[11] M. A. Stebbins, J. R. Blough, S. J. Shelly, and D. L. Brown, "Multi-axis Load Cell Calibration and Determination of Sensitivities to Forces and Moments", *International Modal Analysis Conference*, 1997.

[12] N. Ulbrich, "Hidden Connections between Regression Models of Strain-Gage Balance Calibration Data", *AIAA Paper 2013-1018*.

[13] N. Ulbric and R. Gisler, "A Baseline Load Schedule for the Manual Calibration of a Force Balance", *AIAA Paper 2013-1017*.

[14] W. Zhou and D. Chelidze, "Generalized Eigenvalue Decomposition in Time Domain Modal Parameter Identification", *Journal of Vibration and Acoustics*, vol. 130, 2008.